論文 / 著書情報
Article / Book Information

題目(和文)	
Title(English)	Electrodeposition of Ni-Co and Ni-B Alloys and Their Micro-Mechanical Property Characterization
著者(和文)	JiangYiming
Author(English)	Yiming Jiang
出典(和文)	学位:博士(工学), 学位授与機関:東京工業大学, 報告番号:甲第12551号, 授与年月日:2023年9月22日, 学位の種別:課程博士, 審査員:CHANG TSO-FU,曽根 正人,細田 秀樹,木村 好里,多田 英司,田原 正樹,HSU YUNG JUNG
Citation(English)	Degree:Doctor (Engineering), Conferring organization: Tokyo Institute of Technology, Report number:甲第12551号, Conferred date:2023/9/22, Degree Type:Course doctor, Examiner:,,,,,,
学位種別(和文)	博士論文
Type(English)	Doctoral Thesis

Electrodeposition of Ni-Co and Ni-B Alloys and Their Micro-Mechanical Property Characterization

Doctor of Engineering

Department of Materials Science and Engineering

School of Materials and Chemical Technology

Tokyo Institute of Technology

Yiming Jiang

2023

Table of Contents

CHAPTER 1

General Introduction

1-1. Background

1-1-1. Electrodeposition of Ni alloys

Electrodeposition is an important method to produce metallic coatings by applying electric current or potential on a conductive material immersed in a solution containing a salt of the metal to be deposited. Electrodeposition is widely applied in fabrication of electronic components because of the ease in controlling the morphology, crystal structure, composition and deposition rate of the electrodeposited materials [1-1~1-4]. For electrodeposition of Ni alloys, their property could be manipulated simply by varying the electrodeposition parameters, such as the current density, bath composition, additives and temperature [1-5, 1-6]. For instance, the grain size and composition of alloys could be controlled by changing the current density, pulsed electrodeposition, the use of ultrasound [1-7], or the use of additives [1-8] such as brighteners [1-9]. Electrodeposition is particularity effective in refining the average grain size to nanoscale and decoration of non-uniform surfaces [1-10], which are advantageous in fabrication of electronic components. By integrating electrodeposition technique with lithography process, three dimensional components or metallic micro-patterns can be

rapidly fabricated, and the production method is already applied in manufacturing process of MEMS devices [1-11~1-13].

Electroless deposition and electrodeposition and physical vapour deposition techniques (e.g. sputtering) are also common methods applied in fabrication of Ni alloy films. However, physical vapour deposition methods are known to involve complex processing sequence and high process cost. Electroless deposition and electrodeposition methods are easily adoptable for production of electronic components because of the low production cost and simple process. Among the two deposition methods, electrodeposition offers a higher deposition rate, better crystallinity, higher stability of the electrolyte and more uniform distribution of the second element in the metal matrix when comparing with the electroless deposition method. For instance, the deposition rate in electrodeposition is reported to be up to 600 times higher than the deposition rate in electroless deposition [1-14]. Ni-B alloy deposition through an electroless method also suffers from a low bath life.

Nickel-cobalt alloys are important functional materials due to their unique magnetic and mechanical properties, and these characteristics could be well manipulated when electrodeposition is applied [1-15~1-17]. The nickel-cobalt system has shown advantageous properties compared to other ferrous metals, such as that the magnetic characteristics can be shifted from soft magnetic to permanent magnetic for cobalt rich alloy deposits [1-18]. Moreover, the electrodeposition process can be integrated with photolithography process for fabrication of components in miniaturized electronic devices, such as microelectromechanical systems (MEMS) devices [1-19, 1-20]. For example, nickel-cobalt alloys have been applied as the magnetic component

in MEMS actuators [1-21]. An interesting finding in electrodeposition of Ni-Co alloys is that the Co/(Co＋Ni) ratio in the electrodeposited alloy is considerably higher than the ratio in the bath since the less noble constituent, which is cobalt here when compare to nickel, is reduced and electrodeposited preferentially.

Electrodeposited Ni-based materials typically exhibit low thermal stability and lose their high mechanical strengths after annealing at a relatively low temperature, which is a major limitation in their applications. For example, the abnormal grain growth of electrodeposited Ni can be observed after heat treatment of 200 °C for 2 h [1-22]. Incorporation of B is an effective method to enhance the mechanical strength, wear resistance and thermal characteristic of Ni-based materials [1-23]. The formation of intermetallic compounds, such as Ni_3B or Ni_2B, contributes to outstanding mechanical performance by the precipitation strengthening mechanism in Ni-B plating. For instance, Ni-B alloys are regarded as potential electrical contact materials in electronic and semiconductor industries due to their electrical conductivity, erosion resistance and solderability.

1-1-2. Anomalous codeposition

Electrodeposition of iron group metals is recognized to be an anomalous codeposition process in an aqueous electrolyte [1-24]. Regarding the case of Ni-Co, the anomalous behavior is represented by a much higher cobalt content in the deposits than the Co ratio in the electrolyte. Studies have shown the hydrogen evolution reaction (HER) plays an important role in the electrodeposition of iron group metals [1-25]. The electrodeposition of iron-group alloys is followed by a local pH rise near the electrode

surface since H_2 is evolved simultaneously with the reduction of iron-group metal ions. With an increase in the near-cathode concentration of OH^-, metal ions would undergo hydrolysis reaction and lead to the formation and adsorption of metal hydroxide ions on the cathode surface. Due to a higher adsorption ability of the $Co(OH)^+$ than that of the $Ni(OH)^+$ [1-5], the reduction of Co is favored while the reduction of Ni is inhibited. The mechanism is reported as:

$$M^{2+} + OH^- \rightarrow MOH^+ \quad (1\text{-}1)$$

$$MOH^+ \rightarrow MOH_{ads}^+ \quad (1\text{-}2)$$

$$MOH_{ads}^+ + 2e^- \rightarrow M(s) + OH^- \quad (1\text{-}3)$$

where M indicates Ni or Co atoms. Bai et al. have reported controls of the anomalous electrodeposition through the method of pulse-reverse plating and controlling the composition of the electrolyte, pH, electrodeposition potential and time [1-6]. It is reported that the alloy electrodeposition of Ni-Co alloys with a deep eutectic solvent-based electrolyte does not follow the anomalous codeposition process [1-26]. This indicates a different electrodeposition mechanism for non-aqueous baths due to an absence of the HER.

1-1-3. Mechanical property strengthening

Mechanical property characterization of materials applied in electronic devices is necessary for design of the structure components since the reliability and structure stability of the component are highly dependent on the mechanical property. For metallic materials, the mechanical property is closely related to its average grain size

according to the grain boundary strengthening mechanism. When dislocations moving and encountering a grain boundary, atomic mismatch between different grains creates a stress field to oppose dislocation motion. Lower dislocations per grain makes lower pressure at grain boundaries, which makes dislocation propagation harder. In many cases, the microhardness is dependent on the average grain size according to the Hall-Petch relationship. According to the Hall-Petch relationship, significant strengthening in metallic materials is obtained by refining the average grain size to nanoscale (below 100 nm) when compared with coarse-grained counterparts. Some of unique properties observed in nanocrystalline materials including enhanced wear resistance and decreased coefficient of friction are also in part attributed to the grain size effect caused by the increased interfacial defect volume fraction.

Alloying allows utilization of the solid solution strengthening mechanism to allow further enhancement of the mechanical strength [1-27]. When solute atoms are introduced, local stress fields are formed that would interact with the dislocations, impeding their motion and causing an increase in the mechanical strength. Usually, the solid solution strengthening mechanism observed in nanocrystalline alloys is expected to be the same as that in a coarse-grain alloy, and strengthening effect is known to be mostly depended on composition in a binary alloy system. For Ni-Co alloys, Ni and Co form a solid solution over the whole concentration range due to their close element numbers and similar atom structures, which makes the alloy promising in manipulating the property toward practical applications.

1-1-3. Specimen size effect

The strengths of metallic materials are known to be dependent on the specimen sizes on micro-scale or nano-scale, which is known as the specimen size effect [1-28~1-30]. For example, in single crystal face centered cubic metals, the strengthening is observed when the extrinsic sample dimensions are reduced below the required distance for dislocation self-duplication. In this case, the conventional dislocation propagation mechanism ceases and the materials are left in a "dislocation-starved state", making the deformation process harder and leading to a size-dependent strength response (Greer et al., 2005) [1-31]. The effect can be described by a power law dependence, $\sigma \propto D^{-n}$, where σ is the strength, D is the specimen size and n is a scaling exponent.

In design of structure components in electronic devices, the mechanical property characterization is critical to understand the reliability and structure stability of the structure component. Thus, the specimen size effect has to be considered in the design of micro-scale components in miniaturized devices, such as micro-electro-mechanical system (MEMS) devices.

1-2. Thesis objective

In this thesis, Ni-Co and Ni-B alloy films were fabricated by eletrcodeposition method. Electrodeposition provides controlling over the morphology, crystal structure, composition and deposition rate of the electrodeposited materials. For electrodeposition of Ni alloys, their property are manipulated simply by varying the electrodeposition parameters, such as the current density, bath composition, additives and temperature.

Especially the effects of additive NaBr on the Ni-Co electrodeposition are studied in this work, the cathode reduction process is also investigated by electrochemical analytic methods.

Alloy electrodeposition allows the utilization of grain boundary strengthening, solid solution strengthening and precipitation strengthening mechanism to realize the enhancement of their mechanical strength. Emerging focused ion beam milling and micro-mechanical testing technology provide ways for precise evaluation of the mechanical property on micro- and nano-scale. The micro-mechanical strength and deformation behaviors of Ni alloys are investigated through micro-compression tests.

1.3 Thesis overview

To accomplish the objectives of this thesis, the following chapters are established.

In Chapter 1, backgrounds of electrodeposition process, applications of Ni-Co and Ni-B alloys and mechanical property characterization are addressed. After the background, the motivation and objective of this thesis are described.

In Chapter 2, effects of the applied current density and additives on the average grain size, composition, and mechanical properties of electrodeposited Ni-Co alloy deposits are evaluated. The strengthening effects related to the composition and grain size are discussed.

In Chapter 3, the mechanical properties of nickel-cobalt alloys on the micro-scale were evaluated for the application as micro-components in miniaturized electronic devices. The mechanical properties on the micro-scale were evaluated by

micro-compression test using micro-pillar type specimens fabricated by focused ion beam system to take the sample size effect into consideration. The yield strength of the nickel-cobalt alloy revealing influences from the sample size, grain boundary strengthening and solid-solution strengthening effects.

In Chapter 4, effects of the bromide ions in Ni-Co electrodeposition are investigated by electrochemical analytical methods, such as cyclic voltammetry and linear sweep voltammetry. Effects of the pH are also examined since formation of the metal hydroxides plays an important role in the Ni-Co alloy electrodeposition.

In Chapter 5, Ni-B alloy films with the B content ranged from 2.8 at.% to 14.3 at.% were electrodeposited by controlling the current density. Micro-compression test was conducted to appraise the micro-mechanical strength. The mechanical strength and deformation behavior are determined by the micro-compression test. In addition, effects of the heat treatment on the crystalline structure and mechanical properties of the electrodeposited Ni-B alloy films are evaluated to clarify the thermal stability.

In Chapter 6, the specimen size effect on mechanical properties of electrodeposited nickel-boron alloys is evaluated by micro-compression test using non-tapered pillar type micro-specimens. The mechanical strength is determined from the engineering stress-engineering strain curve generated from the micro-compression test. Micro-specimens with different sizes are fabricated from the as-electrodeposited and annealed Ni-B alloys by focus ion beam system.

References

1-1. T. Yamamoto, K. Igawa, H. C. Tang, C. Y. Chen, T. F. M. Chang, T. Nagoshi, O. Kudo, R. Maeda, M. Sone, Microelectron. Eng. 213 (2019) 18-23.

1-2. T. Nagoshi, T. F. M. Chang, S. Tatsuo, M. Sone, Microelectron. Eng. 110 (2013) 270-273.

1-3. X. Luo, C. Y. Chen, T. F. M. Chang, H. Hosoda, M. Sone, J. Electrochem. Soc. 162 (2015) D423-D426.

1-4. T. Homma, Y. Kita, T. Osaka, J. Electrochem. Soc. 147 (2000) 4138-4141.

1-5. A. Bai, C.C. Hu, Electrochim. Acta 47 (2002) 3447-3456.

1-6. C.C. Hu, C.K. Wang, Electrochim. Acta 51 (2006) 4125-4134.

1-7.I. Tudela, Y. Zhang, M. Pal, I. Kerr, A.J. Cobley, Surf. Coat. Tech. 259 (2014) 363-373.

1-8. M. Hakamada, Y. Nakamoto, H. Matsumoto, H. Iwasaki, Y. Chen, H. Kusuda, M. Mabuchi, Mater. Sci. Eng. A 457 (2007) 120-126.

1-9. K. Tanaka, M. Sakakibara, H. Kimachi, Procedia Eng. 10 (2011) 542-547.

1-10. U. S. Waware, A. M. S. Hamouda, N. P. Wasekar, *Surf. Coat. Technol.*, 337 (2018) 335-341.

1-11. S. Ghosh, *Thin Solid Films*, 669 (2019) 641-658.

1-12. V. Vitry, J. Hastir, A. Mégret, S. Yazdani, M. Yunacti, L. Bonin, *Surf. Coat. Technol.*, 429 (2022) 127937.

1-13. S. Arai, T. Saito, M. Endo, J. Electrochem. Soc. 154 (2007) D530-D533.

1-14. S. Arai, K. Miyagawa, ECS J. Solid State Sci. Technol. 2 (2013) M39-M43. https://doi.org/10.1149/2.036311jss.

1-15. N. Huang, D. W. Kirk, S. J. Thorpe, C. Liang, L. Xu, S. Zhang, W. Li, M. Sun, ECS Trans. 61 (2014) 9-13.

1-16. P. C. Andricacos, Electrochemically Deposited Thin Films II, M. Paunovic, Editor, The Electrochemical Society Proceedings Series, Pennington, NJ, 1995.

1-17. T. Horiuchi, Y. Furuuchi, R. Nakamura, K. Hirota, Microelectron. Eng. 83 (2006) 1316-1320.

1-18. M. Duch, J. Esteve, E. Gómez, R. Pérez-Castillejos, E. Vallés, J. Micromech. Microeng. 12 (2002) 400-405.

1-19. B. Lochel, A. Maciossek, Electrodeposited Magnetic Alloys for Surface Micromachining, J. Electrochem. Soc. 143 (1996) 3343-3348.

1-20. E. Pellicer, A. Varea, K. M. Sivaraman, S. Pane, S. Surinach, M. D. Baro, J. Nogues, B. J. Nelson, J. Sort, *ACS Appl. Mater. Interfaces*, **3**, 2265 (2011).

1-21. K. Krishnaveni, T. S. N. Sankara Narayanan, S. K. Seshadri, *J. Alloys Compd.*, 480 (2009) 765-770.

1-22. K. M. Gorbunova, M. V. Ivanov, V. P. Moiseev, *J. Electrochem. Soc.*, 120 (1973) 613.

1-23. N. Yu, Bekish, S. K. Poznyak, L. S. Tsybulskaya, T. V. Gaevskaya, *Electrochim. Acta*, 55 (2010) 2223-2231.

1-24. S. Goldbach, R. de Kermadec, F. Lapicque, J. Appl. Electrochem. 30 (2000) 277-284.

1-25. C. K. Chung, W. T. Chang, Thin Solid Films 517 (2009) 4800-4804.

1-26. Y. Tsuru, M. Nomura, F.R. Foulkes, J. Appl. Electrochem. 32 (2002) 629–634.

1-27. Y. H. You, C. D. Gu, X. L. Wang, J. P. Tu, Surf. Coat. Technol. 206 (2012) 3632-3638.

1-28. H. Tang, T.F.M. Chang, Y.W. Chai, C.Y. Chen, T. Nagoshi, D. Yamane, H. Ito, K. Machida, K. Masu, M. Sone, J. Electrochem. Soc. 165 (2018) D58-D63.

1-29. M. D. Uchic, D. M. Dimiduk, J. N. Florando, W. D. Nix, Science 305 (2004) 986-989.

1-30. D. Kiener, W. Grosinger, G. Dehm, R. Pippan, Acta Mater. 56 (2008) 580-592.

1-31. J. R. Greer, W. C. Oliver, W. D. Nix, Acta Mater. 53 (2005) 1821-1830.

CHAPTER 2

Electrodeposition of Ni-Co Alloy Deposits

2-1. Introduction

Electrodeposition is widely applied in fabrication of metallic materials because of the ease in controlling the morphology, crystal structure, composition and deposition rate of the electrodeposited materials. For electrodeposition of Ni-Co alloys, the property could be manipulated simply by varying the electrodeposition parameters, such as the current density, bath composition, and temperature [2-1, 2-2]. For instance, the grain size of alloys could be controlled by changing the current density, pulsed electrodeposition, the use of ultrasound [2-3], or the use of additives [2-4] such as brighteners [2-5]. An interesting finding in electrodeposition of Ni-Co alloys is that the Co/(Co＋Ni) ratio in the electrodeposited alloy is considerably higher than the ratio in the bath since the less noble constituent, which is Co here when compare to Ni, is reduced and electrodeposited preferentially [2-1]. Electrodeposition is particularity effective in refining the average grain size to nanoscale and decoration of non-uniform surfaces [2-6], which are advantageous in fabrication of electronic components [2-7]. By integrating electrodeposition technique with lithography process, three dimensional

components or metallic micro-patterns can be rapidly fabricated, and the production method is already applied in manufacturing process of MEMS devices [2-8].

2-2. Experimental

Ni-Co alloys were electrodeposited from a sulfamate-based bath. The bath was composed of 270 g/L $Ni(SO_3NH_2)_2 \cdot 4H_2O$, 30 g/L $Co(SO_3NH_2)_2 \cdot 4H_2O$, and 40 g/L H_3BO_3, 10 g/L $NiBr_2$ and 0.5 vol.% NSF-E, which was a surface brightener provided by Nihon Kagaku Sangyo Co., Ltd., Japan. The bath was kept at 50 ℃ and kept stirring using a magnetic stirrer during electrodeposition. Direct currents with the current density ranged from 5 to 20 mA/cm^2 were applied. The Ni-Co alloys were electrodeposited on 99.96% copper substrates (Kikuya PM Co., Ltd.) in a size of 10×10 mm^2. A piece of 99.95% platinum plate (Kikuya PM Co., Ltd.) was used as the counter electrode. A schematic of the electrodeposition is shown in Fig. 2-1. Crystalline structure of the Ni-Co alloy deposits was characterized by X-ray diffraction (XRD, Ultima IV, Rigaku Corp., Tokyo, Japan), the X-ray was generated by a copper target operated at 40 kV and 40 mA. The average grain size (d) was determined using the XRD result in conjunction with the Scherrer equation.

Microhardness tests were conducted on a micro hardness tester (HMV-G20S, Shimadzu Corp., Kyoto, Japan) using a load of 0.100 kg (HV 0.100), and a loading time of 15 s. Microhardness results reported were average values of 5 points located in the center and four corners of the alloy deposit. The Ni-Co alloy electrodeposited copper substrates were cut into slices to show cross-section of the deposits. The surface morphology and microstructure of the alloy deposits were

investigated using a scanning electron microscope (SEM, SU4300SE Hitachi Co., Ltd., Japan). The composition was analyzed by energy dispersive X-ray spectroscopy system (EDX, EMAX EX-250 Horiba Co., Ltd., Kyoto, Japan) equipped in the SEM.

2-3. Grain size and composition of Ni-Co alloy deposits

Ni-Co alloys, pure Ni and Co deposits obtained in this study all exhibit XRD peaks corresponding to the (111), (200), and (220) planes in the face-centered cubic (FCC) structure as shown in Fig. 2-2. The (111) diffraction peak was the highest for all the Ni-Co alloys. Average grain sizes of these alloys were estimated from the (111) diffraction peaks using the Scherrer equation.

Grain sizes of the Ni-Co alloy deposits obtained from the bath containing no additive (A samples, ●) increased as the current density increased as shown in Fig. 2-3. Grain refinement was observed after addition of $NiBr_2$ (B samples, ■) into the bath. For instance, the grain size decreased from 21.6 to 19.2 nm after addition of $NiBr_2$ when 5 mA/cm^2 was used. Halides, such as bromide in this study, are reported to act like a weak suppressor in electrodeposition that would cause an increase in the overpotential of reduction reactions [2-9, 2-10], and an increase in the overpotential would favor the nucleation and leads to grain refinement of the deposit [2-11]. For the Ni-Co alloys obtained from $NiBr_2$-containing bath, the grain size firstly increased and then decreased when varying the current density from 5 to 20 mA/cm^2. The initial increase may be due to higher grain growth rate by increasing current density. Then, the reduction in grain size may also be related to higher overpotential, which would cause an increase in nucleation rate with high current density. NSF-E is a surface brightener, and surface

brightener are also one type of suppressors that causes the grain refinement effect. Hence, further grain refinement was observed in the Ni-Co alloy deposits after addition of the NSF-E.

Co content in the Ni-Co alloy deposits increased as the current density increased when using the bath without the two additives as shown in Fig. 2-4. The standard reduction potential of Co (-0.28 V vs SHE [2-12]) is more negative than that of Ni (-0.257 V vs SHE [2-12]). Therefore, it is expected to see an increase in the Co content following an increase in the current density. For the Ni-Co alloys electrodeposited with the bath containing $NiBr_2$, Co content in the alloy deposit significantly increased from roughly 20 to 60 at.% when compared with A samples. This result again revealed that bromide ions in the bath would work like the suppressor to cause an increase in the overpotential that favors reduction of cobalt. Regarding the effect of current density in B samples, the Co content decreased as the current density increased. This tendency was unexpected, but similar results were reported in Ni-Co alloys electrodeposited from a bath containing the suppressors [2-13]. Ni-Co alloys obtained from the bath containing both $NiBr_2$ and NSF-E had a higher Co content than those in B samples electrodeposited at the same current density, and the Co content also slightly decreased as the current density increased.

As shown in Fig. 2-5, surface morphologies of Ni-Co alloys electrodeposited without addition of the two additives showed granular morphology, and no obvious change was observed when increasing the current density from 5 to 10 mA/cm^2. In Fig. 2-6(a), the Ni-Co alloy deposit electrodeposited with the bath containing $NiBr_2$ showed plate-like morphology when the current density was at 5 mA/cm^2. The morphology

changed to a mixture of edge-rich morphology and granular particles as the current density increased to 10 mA/cm^2. Then, as the current density increased to higher than 12 mA/cm^2, the morphology became granular particles completely as shown in Fig. 2-6(c) and (d). The change from plate-like morphology to granular morphology as the current density increased could be explained by the classic nucleation model. The surface energy of crystalline solids is usually anisotropic, and the applied potential involved in the reduction reaction would be lowered as the current density lowered according to the Butler-Volmer equation. This implies at a low current density, the Ni-Co alloy would have a preferred growth direction that leads to the edge-rich morphology, however, the energy involved in reduction of Ni-Co alloy could be high enough to result the granular morphology at a high current density. After addition of the brightener (NSF-E), the surface of both (NSF-E, Br^-) and (NSF-E) samples became smooth and showed no sign of uniform granular particles as shown in Fig. 2-7.

2-4. Hardness of Ni-Co alloy deposits

The hardness values versus the average grain sizes were plotted in Fig. 2-8. Refinement in the average grain size was observed after introduction of the surface brightener (NSF-E) when comparing results between the alloys electrodeposited with the bath only (yellow cross symbol) and with the NSF-E (black diamond symbol). The same trend was observed between the $NiBr_2$ case (blue cycle symbol) and the $NiBr_2$+NSF-E case (orange triangle symbol). For instance, the grain size decreased from 20.9 to 13.6 nm after addition of NSF-E into the sulfamate bath when a current density of 20 mA/cm^2 was used.

Generally, strengthening in the Ni-Co alloys was observed as the grain size reduced in this study, which revealed contribution of the grain boundary strengthening mechanical. Data points located at the left of the figure, that is the fine grain size region, showed relatively higher micro-hardness values. The tendency followed the Hall-Petch relationship well.

As shown in Fig. 2-9, values of the Co content in the Ni-Co alloys were all higher than the concentration of Co ions in the sulfamate bath. It is reported that the Co/(Co+Ni) ratio in the deposits is considerably higher than the ratio in the bath in electrodeposition of Ni-Co alloys since the less noble constituent in the bath, which is Co in this study when compare to Ni, tends to be reduced and electrodeposited preferentially. After addition of the surface brightener, NSF-E, the Co content increased by ca. 20 at.%.

On the other hand, the effect of $NiBr_2$ on the Co content was unexpected. The Co content in the deposit significantly increased from roughly 20 to 60 at.% when comparing between the alloy obtained with the sulfamate bath only and the $NiBr_2$ cases. An obvious increase in the Co content was also observed when adding $NiBr_2$ into the bath containing NSF-E as shown in Fig. 2-9. Hence the change was suggested to be caused by the bromide ions. Bromide ions in the bath could work like the suppressor to cause an increase in the applied potential that favors reduction of cobalt.

Generally, the micro-hardness increased following an increase in the Co content as shown in Fig. 2-9, which reveal the strengthening contributed by the solid-solution strengthening mechanism. Besides, a relatively fine grain size and low Co content was

obtained for the alloy deposited with only the NSF-E (black diamond symbol), and still, it showed a high micro-hardness value within this study which is closer to the alloys obtained with NSF-E+$NiBr_2$ (orange triangle symbol). This finding indicated a stronger contribution from the grain boundary strengthening on the overall mechanical strength than that from the solid solution strengthening.

2-5. Chapter Summary

Ni-Co alloy deposits were electrodeposited in a sulfamate bath. The Ni-Co alloy deposits showed granular morphology except the one electrodeposited with the bath containing $NiBr_2$ and the current density at 5 mA/cm^2, which the surface showed plate-like morphology. Refinement in the average grain size was observed after introduction of $NiBr_2$ and a surface brightener (NSF-E) into the bath. The Co content increased from ca. 20 to 60 at.% after addition of $NiBr_2$ and NSF-E into the bath. The microhardness was confirmed to be affected by both of the grain size and the Co content, and the dependency was higher on the grain size. The microhardness reached 862.2 Hv in a Ni-Co alloy deposit having 13.0 nm grain size and 66.64 at.% Co content.

References

2-1. A. Bai and C.C. Hu, Effects of electroplating variables on the composition and morphology of nickel-cobalt deposits plated through means of cyclic voltammetry, Electrochim. Acta 47 (2002) 3447-3456.

2-2. C.C. Hu and C.K. Wang, Effects of composition and reflowing on the corrosion behavior of Sn-Zn deposits in brine media, Electrochim. Acta 51 (2006) 4125-4134.

2-3. I.Tudela, Y. Zhang, M. Pal, I. Kerr, A.J. Cobley, Ultrasound-assisted electrodeposition of composite coatings with particles, Surf. Coat. Tech. 259 (2014) 363-373.

2-4. M.Hakamada, Y. Nakamoto, H. Matsumoto, H. Iwasaki, Y. Chen, H. Kusuda, M.Mabuchi, Relationship between hardness and grain size in electrodeposited copper films, Mater. Sci. Eng. A 457 (2007) 120-126.

2-5. K. Tanaka, M. Sakakibara, H. Kimachi, Grain-size effect on fatigue properties of nanocrystalline nickel thin films made by electrodeposition, Procedia Eng. 10 (2011) 542-547.

2-6. D.-Y.Park, K.S. Park, J.M. Ko, D.-H. Cho, S.H. Lim, W.Y. Kim, B.Y. Yoo, N.V.Myung, Electrodeposited $Ni_{1-x}Co_x$ Nanocrystalline Thin Films: Structure-Property Relationships, J. Electrochem. Soc. 153 (2006) C814-C821.

2-7. N.V.Myung, D.Y. Park, B.Y. Yoo, P.T.A. Sumodjo, Development of electroplated magnetic materials for MEMS, J. Magn. Magn. Mater. 265 (2003) 189-198.

2-8. K. Nitta, T.F.M. Chang, H. Tang, C.Y. Chen, S. Iida, D. Yamane, K. Machida, H. Ito, K. Masu, M. Sone, Alloy electroplating and Young's modulus characterization of AuCu alloy microcantilevers, J. Electrochem. Soc. 167 (2020) 082503.

2-9. Y. Tsuru, M. Nomura, F.R. Foulkes, Effects of chloride, bromide and iodide ions on internal stress in films deposited during high speed Ni electroplating from a Ni sulfamate bath, J. Appl. Electrochem. 30 (2000) 231-238.

2-10. T.M.T. Huynh,; F. Wess,; N.T.M. Hai,; W. Reckien,; T. Bredow,; Fluegel, A.; Arnold, M.; Mayer, D.; Keller, Hu.; Broekmann, P. On the role of halides and thiols in additive-assisted copper electroplating. Electrochim. Acta 2013, 89, 537-548.

2-11. Moti, E.; Shariat, M.H.; Bahrololoom, M.E. Influence of cathodic overpotential on grain size in nanocrystalline Ni deposition on rotating cylinder electrodes. J Appl. Electrochem. 2008, 38, 605-612.

2-12. Vanýsek, P. Electrochemical series. In Handbook of Chemistry and Physics, 93rd ed.; Haynes, W.M. Eds.; CRC Press. New York, USA, 2012, pp. 5-88.

2-13. Burzyńska, L.; Rudnik, E. The influence of electrolysis parameters on the composition and morphology of Co–Ni alloys. Hydrometallurgy 2000, 54, 133-149.

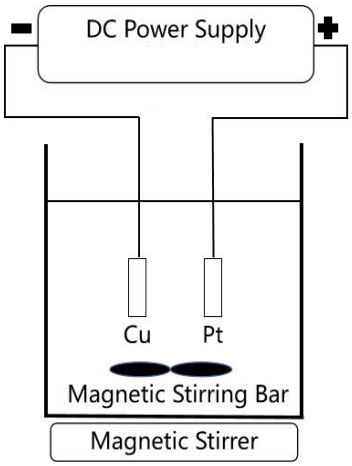

Fig. 2-1 The schematic of the electrodeposition process.

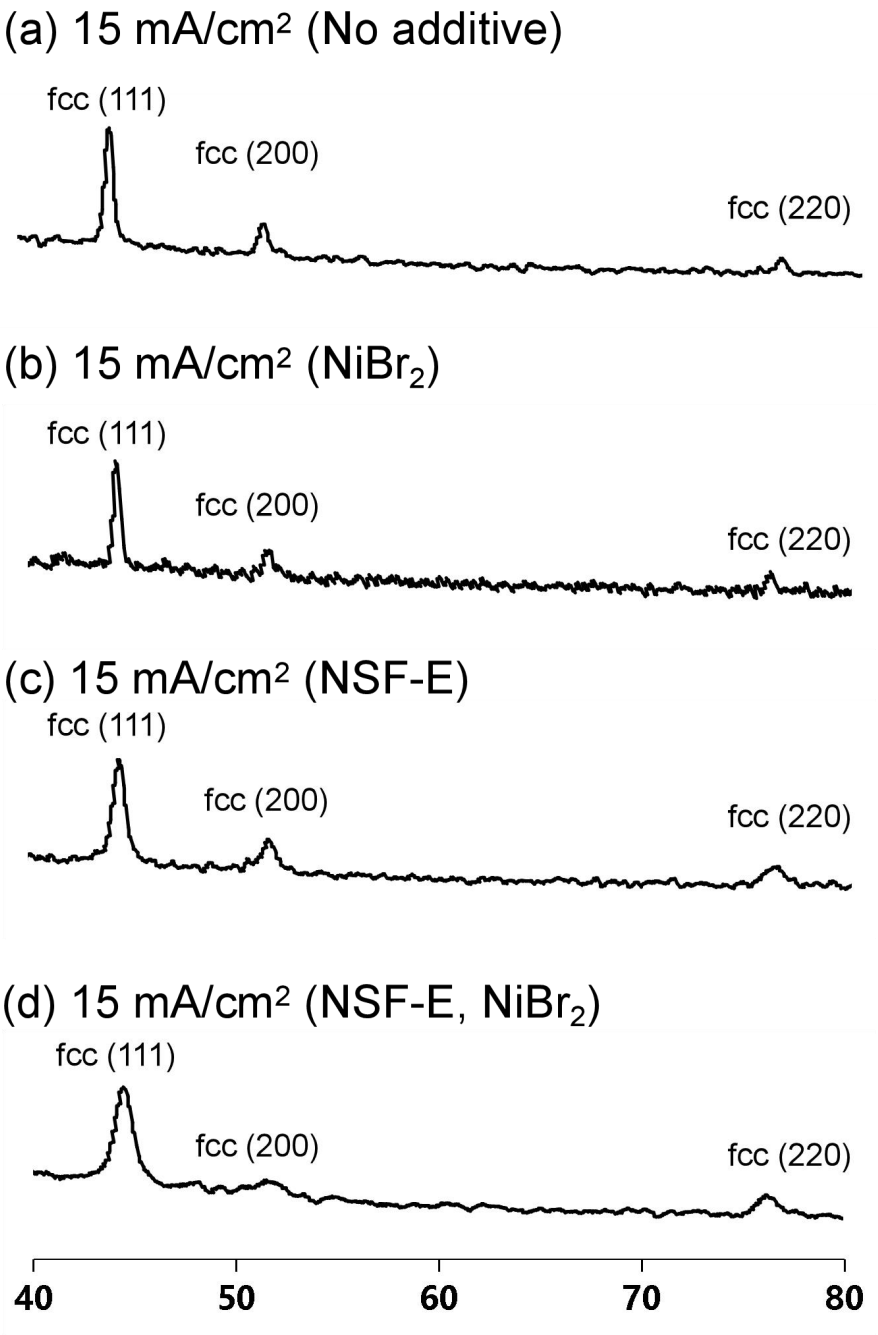

Fig. 2-2 XRD patterns of Ni-Co alloys deposited with current density at 15 mA/cm^2 and the bath containing (a) no additives, (b) $NiBr_2$, (c) NSF-E and (d) both $NiBr_2$ and NSF-E.

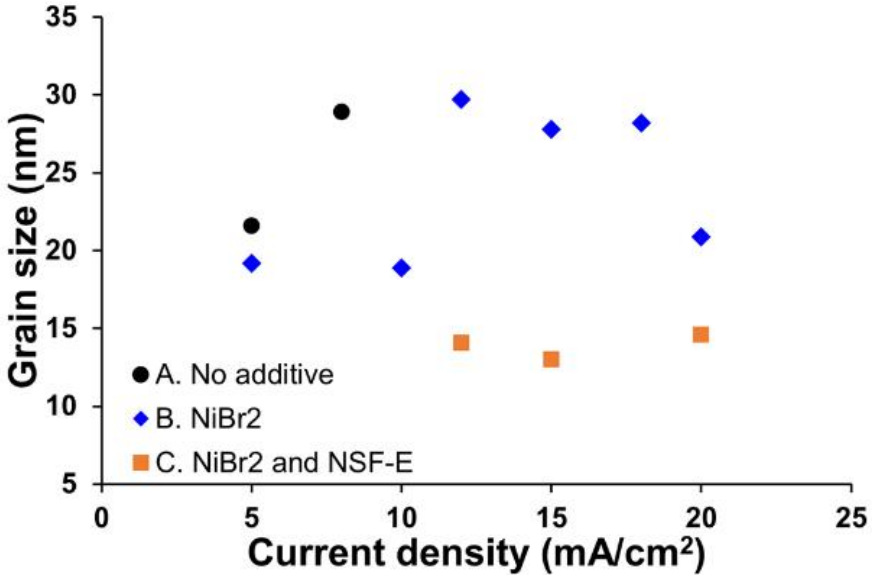

Fig. 2-3 The relationship between the current density and grain size.

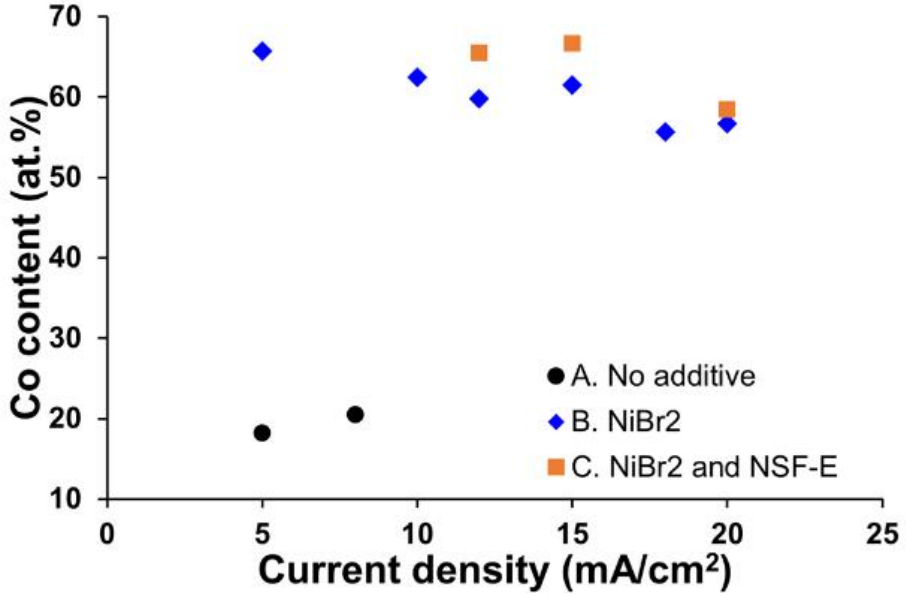

Fig. 2-4 The relationship between the current density and Co content.

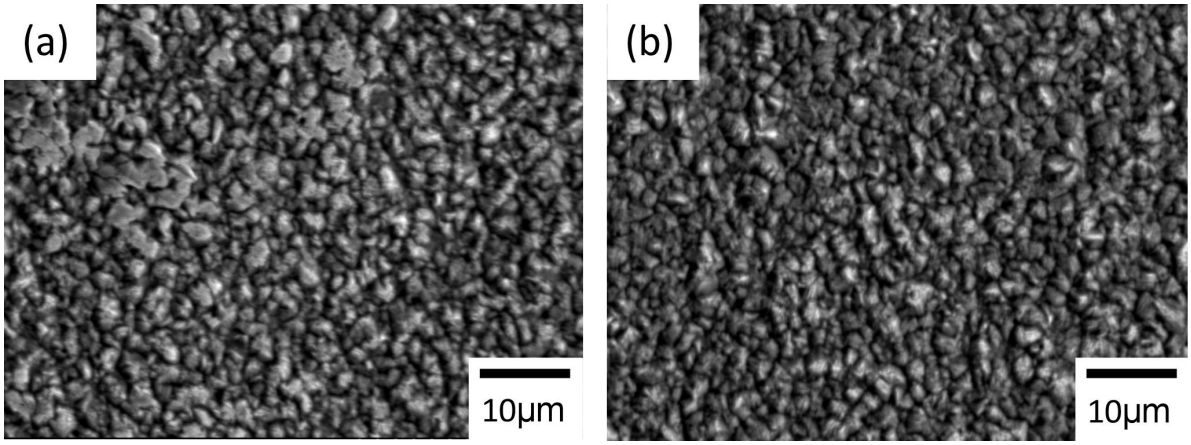

Fig. 2-5 SEM images of Ni-Co alloys electrodeposited without the additives at (a) 5 and (b) 10 mA/cm^2.

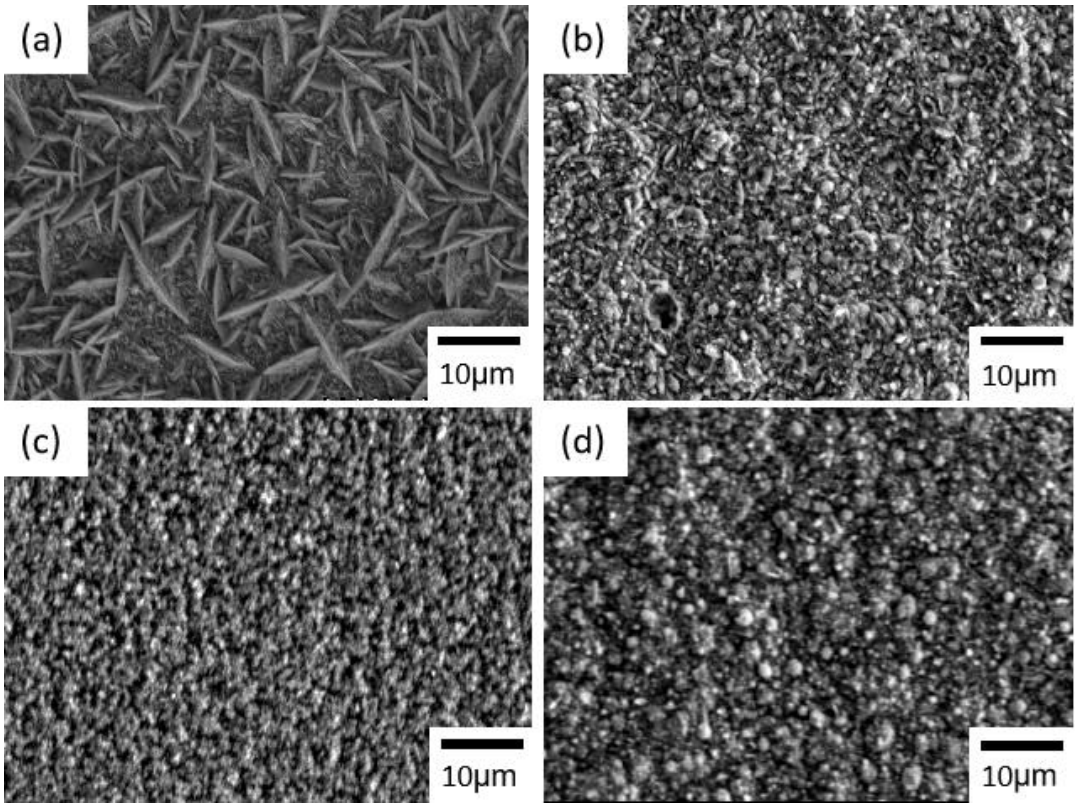

Fig. 2-6 SEM images of Ni-Co alloys electrodeposited with the bath containing $NiBr_2$ and current density at (a) 5, (b) 10, (c) 12 and (d) 20 mA/cm^2.

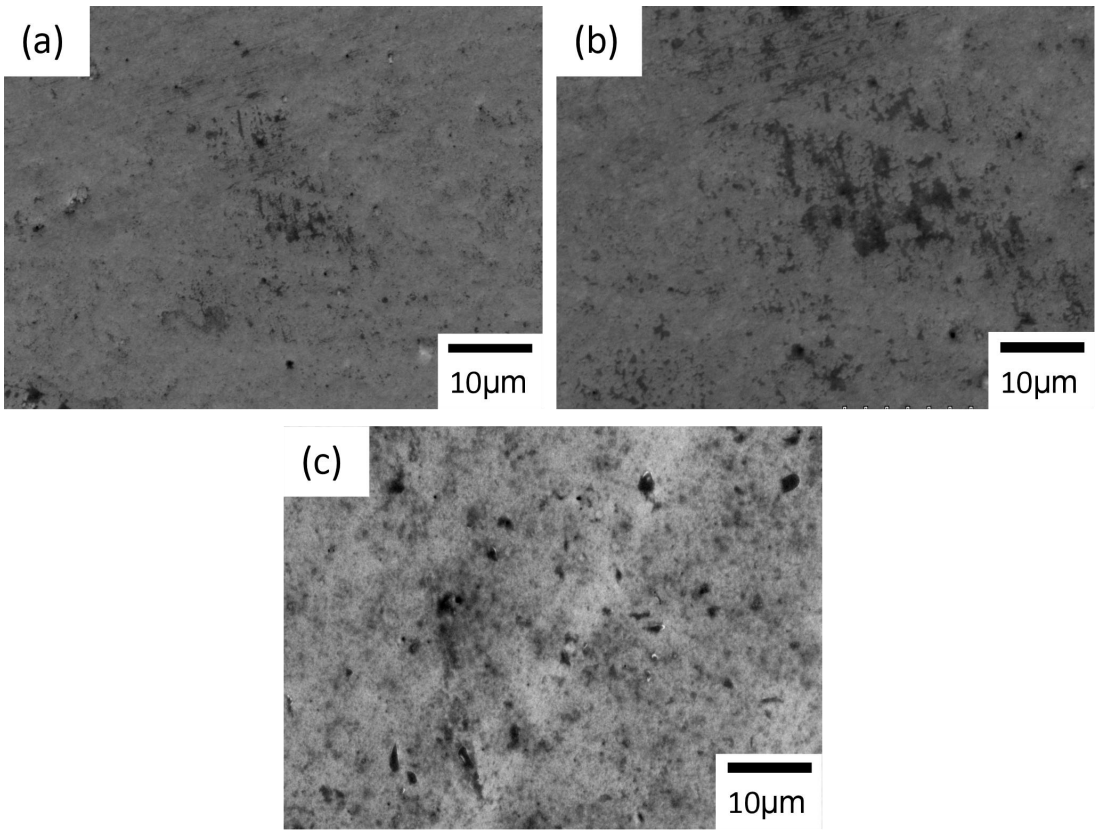

Fig. 2-7 SEM images of Ni-Co alloys electrodeposited with the bath containing both $NiBr_2$ and NSF-E and current density at (a) 12, (b) 15 mA/cm^2 and (c) containing only NSF-E at 15 mA/cm^2.

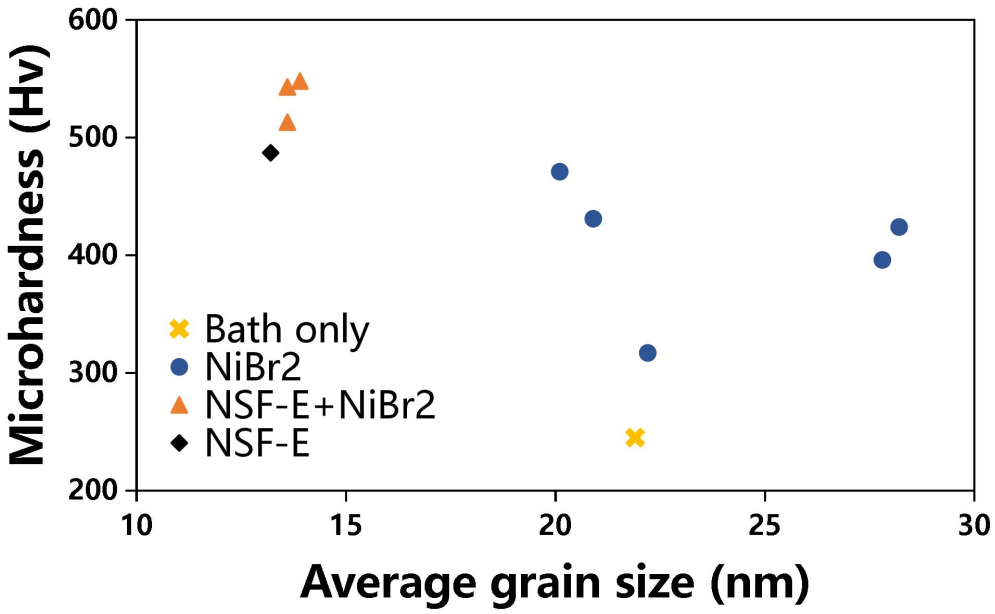

Fig. 2-8 The relationship between the average grain size and micro-hardness.

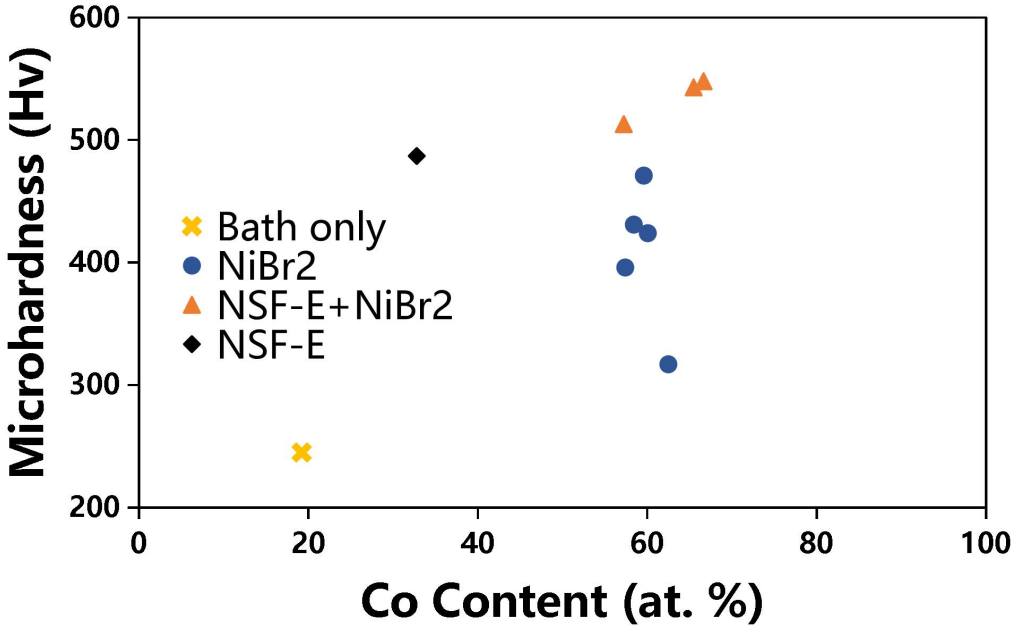

Fig. 2-9 The relationship between the Co content and micro-hardness.

CHAPTER 3

Anomalous Codeposition of Ni-Co Alloys and Effects of Bromide Ions

3-1. Introduction

With the growing demand for more efficient production of industrial electronic devices, high speed electrodeposition is regarded as an important technique for manufacturing of components in electronic devices. For instance, electrodeposition can be integrated with photolithography process to fabricate micro-gears and memory devices [3-1~3-3]. Ni-Co alloys are promising materials toward electronic components because of the excellent magnetic, mechanical, and corrosion properties, and these properties of Ni-Co alloys are highly dependent on their composition and micro-structure. For Ni-Co alloys prepared by electrodeposition, the composition and micro-structure could be manipulated by controlling process variables such as pH, additives, and applied current density [3-4~3-8].

Electrodeposition of Ni-Co is known to be an anomalous codeposition process in an aqueous electrolyte. The anomalous behavior is represented by a much higher cobalt content in the deposits than the Co ratio in the electrolyte. It has been reported that the hydrogen evolution reaction plays an important role in the electrodeposition of iron group metals.

Halide ions are used as weak suppressors in the electrodeposition of iron group metals to improve the deposit quality [3-9]. Bromide ions are reported to promote the dissolution of the anode by destabilizing the passive film on its surface and lower the internal stress of the deposits [3-10]. In case of the alloy electrodeposition of Ni-Co alloys, the Co content was confirmed to greatly increase after the addition of bromide ions ($NiBr_2$) in a previous work [3-11]. Addition of nickel ions into the electrolyte is expected to cause an increase in the nickel content in the deposits. However, an unexpected result was obtained. Therefore, the increased cobalt content is suggested to be caused by the increased bromide ion concentration.

The effects of bromide ions in alloy electrodeposition of Ni-Co alloys are interesting, but the mechanism is still not clarified. In this study, NaBr is used as the additive in the alloy electrodeposition to maintain a constant nickel ion concentration in the electrolyte. Effects of the bromide ions are investigated by electrochemical analytical methods, such as cyclic voltammetry and linear sweep voltammetry. Effects of the pH on the alloy electrodeposition are also examined.

3-2. Experimental

The alloy electrodeposition was conducted by the galvanostatic method, and continuous stirring of the bath with a cross-shape magnetic stirrer was conducted. 99.96% copper plates (Kikuya PM Co., Ltd., Tokyo, Japan) were used as the substrates in the alloy electrodeposition. The reaction time was 30 min. The substrates were pretreated in 0.1 M hydrochloric acid (Kanto Chemical Co., Inc., Tokyo, Japan) for 1 min to remove contaminants on the surface, such as oxides. The anode electrode was a

99.95% platinum plate (Kikuya PM Co., Ltd., Tokyo, Japan). The alloy electrodeposition was performed at 50 ℃ with a sulfamate-based bath. $Ni(SO_3NH_2)_2$, $Co(SO_3NH_2)_2$, NaBr and NaCl were all purchased from Kanto Chemical Co., Inc., Tokyo, Japan. Seven types of the electrolyte were prepared to investigate effects of bromide ions. The compositions are provided in Table 1. Unless stated otherwise, pH of the electrolyte was adjusted to 4 in this study. The pH was adjusted by KOH and H_2SO_4 (Kanto Chemical Co., Inc., Tokyo, Japan).

Table 1 Composition of different Ni-Co sulfamate electrolytes.

Electrolyte	$Ni(SO_3NH_2)_2$	$Co(SO_3NH_2)_2$	NaBr	NaCl
No. 1	0.9 M	–	–	–
No. 2	–	0.9 M	–	–
No. 3	0.8 M	0.1 M	–	–
No. 4	0.9 M	–	10 g/L	–
No. 5	–	0.9 M	10 g/L	–
No. 6	0.8 M	0.1 M	10 g/L	–
No. 7	0.8 M	0.1 M	–	10 g/L

Crystalline characteristics of the Ni-Co alloys were evaluated by an X-ray diffractometer (XRD, Ultima IV, Rigaku Corp., Tokyo, Japan). The surface

morphology of the alloy deposits was investigated by a scanning electron microscope (SEM, SU4300SE Hitachi Co., Ltd., Japan). The composition was evaluated by an energy dispersive X-ray analyzer (EDX, EMAX EX-250, Horiba) equipped in the SEM. The current efficiencies were measured by sample weighing before and after galvanostatic electrodeposition at 200 A/m^2. Linear sweep voltammetry (LSV) and cyclic voltammetry (CV) methods were conducted to study the electrochemical characteristics of the alloy electrodeposition. In LSV and CV experiments, the scan rate was set at 10 mV/s unless stated otherwise, the scan range was basically set from -1.2 V to the open circuit potential (-0.4V ~ -0.2V). A Ag/AgCl/saturated KCl electrode was used as the reference electrode, and a Pt plate was used as the counter electrode.

3-3. Surface morphology and Co content

Surface morphologies of the Ni-Co alloys electrodeposited with and without the addition of NaBr are shown in Fig. 1. The alloy deposited without any additives (No. 3 electrolyte) showed a surface morphology of relatively small particle-like structures, and the surface morphology changed to relatively large plate-like structures after the addition of NaBr (No. 6 electrolyte). The change in the surface morphology suggested the nucleus density was lowered or the homogeneous nucleation was promoted after the addition of NaBr. Bromide ions in the electrolyte are expected to work as weak accelerators [3-12, 3-13], and this eventually leads to a lowered nucleus density and the plate-like structures.

The correlation between the Co content and current density in the electrodeposited Ni-Co alloys is plotted in Fig. 2. Values of the Co content were at roughly 30 at.% when

using the sulfamate electrolyte (No. 3 electrolyte) without any additives. The nickel ion concentration in the electrolyte was 8 folds of that of the cobalt ion concentration, and the cobalt/nickel ratio in the deposit was higher than the value in the electrolyte. This result demonstrated the anomalous codeposition behavior. Cobalt is a less noble metal when compared with nickel, and the potential at cathode is expected to be more negative following an increase in the applied current density. Therefore, the Co content is expected to increase following an increase in the applied current density. However, the Co contend was lowered as the current density increased from 100 A/m^2 to 200 A/m^2. This finding confirmed the deposition of metallic nickel and cobalt were not directly from the Ni(II) ions and Co(II) ions in the electrolyte, and generations of the intermediate hydroxides is a possible explanation of the anomalous codeposition behavior. Also, the anomalous codeposition behavior became less predominant when a higher current density is used.

The Co content increased to roughly 60 at.% after the addition of NaBr (No. 6 electrolyte), and it gradually decreased following an increased in the current density, which is similar to the cases without adding any additives. This result confirmed the promoted anomalous codeposition behavior observed in the previous study [17] was caused by the bromide ions. On the contrary, no obvious change in the Co content was observed with the addition of NaCl (No. 7 electrolyte) when compared with the no additive case. This suggested chloride ions could not promote the anomalous codeposition behavior as that observed in the bromide ion case.

Effects of the pH on the Co content is illustrated in Fig. 3. The anomalous codeposition behavior was observed when varying the pH use the electrolyte without

any additives. The Co content slightly decreased following an increase in the pH. Harris et al. have reported a similar trend, which the Ni mass ratio of the deposit decreases at a lower pH in Ni-Fe alloy electrodeposition. Also, by the idea that the intermediate hydroxides play a role in the alloy electrodeposition, this finding is consistent with the Grande and Talbot's model, which a decrease in the pH leads to a decrease in the concentration and reduction rate of nickel hydroxide species [3-14]. After introduction of the NaBr, the decrease in the Co content following an increase in the pH became more obvious, which reveals a low pH environment and the presence of bromide ions resulted a synergistic effect to the anomalous codeposition behavior.

3-4. Crystalline structure

XRD measurement was conducted to characterize the crystalline structure of the Ni-Co alloys. The XRD patterns of the Ni-Co alloys deposited at different pH are shown in Fig. 4. In all alloys, the peaks with the strongest intensity were the peaks at 2θ = ca. 44.5°, which can be indexed to the Ni-Co fcc (111) plane. The other two distinct peaks were indexed to the fcc (200) and fcc (220) at approximately 2θ = 52.0° and 76.5°, respectively. No obvious shift in the peaks was found when varying the pH. The XRD patterns of the alloy obtained from the electrolyte containing NaBr were similar to the case of the electrolyte without any additive. A slight shift in the fcc (111) peak of ca. 0.07° was confirmed as shown in Table 2. This could be explained by the difference in the Co content in the Ni-Co alloys. The XRD peaks were shift toward a lower angle (toward the Co diffraction angle) because of an increase in the Co content after the introduction of bromide ions.

Table 2 XRD Major peak position of the alloys electrodeposited at 200 A/m^2 and various pH with and without the addition of NaBr.

pH	2.0	4.0	8.0	12.0
Additive	Major peak position (°)			
—	44.43	44.47	44.43	44.45
NaBr	44.35	44.38	44.40	44.39

3-5. Electrochemical characteristics

CVs of the six electrolytes (No.1 to No. 6) are shown in Fig. 5. For the pure nickel electrolyte (No. 1 and No. 4) shown in Fig. 5(a), the cathodic current densities decreased after the addition of NaBr. This suggested the bromide ions worked as the suppressor inhibiting the reduction of nickel. This suggestion was supported by the change in the current efficiency. The current efficiency of the pure nickel samples decreased from 89.8% to 86.5% after the addition of NaBr. One interesting finding is that a reduction peak was observed in the range of -0.8 V ~ -1.0 V, and this peak only appeared in the positive sweep. For the pure cobalt, the cathodic current densities slightly increased after introducing bromide ions into the electrolyte as shown in Fig. 5(b), and the current efficiency increased from 89.0% to 90.6%, which confirmed the bromide ions worked as the accelerator in the reduction of cobalt. Regarding the

electrolyte containing both of the nickel and cobalt ions, the accelerator effect was observed after the introduction of bromide ions. In addition, the reduction peak observed in the pure nickel case no longer existed in the alloy electrodeposition. Nickel and cobalt have close standard reduction potentials ($E°_{Ni} = -0.250$ V, $E°_{Co} = -0.277$ V vs. SHE), hence the cathodic current densities were basically at the same level when comparing between the pure nickel, pure cobalt and Ni-Co cases.

In order to clarify the cause of the reduction peak observed in the pure nickel case, CVs were performed with the pure Ni electrolyte without the addition of NaBr at different pH. In Fig. 6(a). the peak disappeared when the pH was at 2. Also, the area between the negative and positive sweeps enlarged following an increase in the pH. This finding suggests that the peak is closely related to the pH and is very likely to be results of the formation and reduction of the nickel hydroxide species. The effect of the scan rate on the reduction of pure nickel was also checked to confirm this. The LSVs are shown in Fig. 7. The reduction peak gradually disappeared as the scan rate decreased from 40 mV/s to 5 mV/s, which indicates the peak is a diffusion limit peak. The intermediate hydroxides are highly active and unstable, and the generation is promoted when there is an increase in the concentration gradient of the OH^- ions from surface of the cathode to the bulk. The concentration gradient is caused by the hydrogen evolution reaction at cathode. Therefore, a higher scan rate leads to a larger concentration gradient of the OH^- ions and the more pronounced reduction peak.

The mechanism of Ni-Co alloy electrodeposition with bromide ions as the additive can be summarized as following: reduction of the nickel and cobalt ions can be shown as:

$$M^{2+} + e^- \rightarrow (M^+)_{ads} \quad (3\text{-}1)$$

$$(M^+)_{ads} + e^- \rightarrow M \quad (3\text{-}2)$$

Besides this basic reaction mechanism, reduction of the noble and active species (Ni^{2+} and Co^{2+} in this case) also happens as:

$$Ni^{2+} + Co^{2+} + e^- \rightarrow [(NiCo)^{3+}]_{ads} \quad (3\text{-}3)$$

$$[(NiCo)^{3+}]_{ads} + e^- \rightarrow Co + Ni^{2+} \quad (3\text{-}4)$$

reaction (3-3) and (3-4) are reductions in which Ni^{2+} and Co^{2+} ions interact with each other. $[(NiCo)^{3+}]_{ads}$ are reported to act as the catalyst to provide another pathway for the electrodeposition of cobalt. The hydroxide species, $[(NiCo)^{3+}]_{ads}$, $(Co^+)_{ads}$ and $(Ni^+)_{ads}$ intermediates would compete for the active sites on cathode, and the competition between these adsorbed intermediate species is considered to be the main cause of the anomalous codeposition behavior.

After the introduction of bromide ions, the anomalous codeposition behavior was further promoted. In reduction of iron group metals involving two consecutive one-electron charge transfers, the participation of anions leads to the formation of adsorbed complexes as following [3-14]:

$$M^{2+} + X^- \rightarrow (M\text{-}X)^+ \quad (3\text{-}5)$$

$$(M\text{-}X)^+ + e^- \rightarrow (M\text{-}X)_{ads} \quad (3\text{-}6)$$

$$(M\text{-}X)_{ads} + e^- \rightarrow M + X^- \quad (3\text{-}7)$$

The anion X^- could be halide ions (Br^-). In the electrodeposition, $(M\text{-}X)^+$ species could also occupy valid active sites on the cathode. It is reported that high-spin cobalt complexes with three unpaired electrons are more labile than that of nickel [3-14]. Hence, the cobalt halide complex is expected to be more active than nickel halide complex formed on the cathode, and explains the preferential reduction of Co^{2+} over that of the Ni^{2+} reduction.

In addition to the above mechanisms, metal-hydrogen codeposition also takes place simultaneously. In the presence of bromide ions, this side reaction can be assumed as [3-15]:

$$(M\text{-}Br)_{ads} + xH^+ + (x\text{-}1)e^- \rightarrow M\text{-}H_x + Br^- \quad (3\text{-}8)$$

Likewise, cobalt intermediate species are more readily absorbed and reduced, resulting in the formation of Co-enriched electrodeposits. This may clarify why lowering the pH of the electrolyte further promoted the anomalous codeposition behavior due to the formation of complexes between cobalt and bromide.

3-6. Chapter Summary

Effects of bromide ions in the Ni-Co alloy electrodeposition were studied. The presence of bromide ions further promoted the anomalous codeposition behavior in Ni-Co alloy electrodeposition, and led to a significant increase in the Co content, which the Co content increased from 30 at.% to 60at.% after the addition of NaBr. The bromide ions were found to work as the accelerator in the reduction of cobalt and suppressed the reduction of nickel. By change pH of the electrolyte, the alloy electrodeposition was confirmed to be affected by the hydroxide intermediates

generated at cathode. The anomalous codeposition behavior was found to be promoted in a lower pH environment. The introduction of bromide ions and the low pH environment resulted a synergistic effect to the anomalous codeposition behavior.

Reference

3-1. D. Golodnitsky, N. V. Gudin, G. A. Volyanuk, Cathode Process in Nickel-Cobalt Alloy Deposition from sulfamate electrolytes — Application to Electroforming, Plating surf. finish. 85 (1998) 65-73.

3-2. T. Horiuchi, Y. Furuuchi, R. Nakamura, K. Hirota, Micro-gear fabrication using optical projection lithography on copper-clad plastic substrates and electroplating of nickel. Microelectron. Eng. 83 (2006) 1316-1320. https://doi.org/10.1016/j.mee.2006.01.083.

3-3. Y. Li, X. Pan, Y. Zhang, X. Chen, Write-Once-Read-Many-Times and Bipolar Resistive Switching Characteristics of TiN/HfO_2/Pt Devices Dependent on the Electroforming Polarity, IEEE Electron Device Lett., 36 (2015) 1149-1152. https://doi.org/10.1109/LED.2015.2477421.

3-4. D. -Y. Park, K. S. Park, J. M. Ko, D. -H. Cho, S. H. Lim, W. Y. Kim, B. Y. Yoo, N. V. Myung, Electrodeposited $Ni_{1-x}Co_x$ Nanocrystalline Thin Films: Structure-Property Relationships, J. Electrochem. Soc. 153 (2006) C814. https://doi.org/10.1149/1.2353792

3-5. T. Fujimura, M. Kunimoto, Y. Fukunaka, T. Homma, Analysis of the hydrogen evolution reaction at Ni micro-patterned electrodes, Electrochim. Acta 368 (2021) 137678 https://doi.org/10.1016/j.electacta.2020.137678.4.

3-6. E. Tamburri, F. Toschi, V. Guglielmotti, E. Scatena, S. Orlanducci, M. Letizia Terranova, Nanofabrication by electrochemical routes of Ni-coated ordered arrays of carbon nanotubes, J. Nanopart. Res. 11 (2009) 1311–1319. https://doi.org/10.1007/s11051-008-9520-y

3-7. T. M. T. Huynh, F. Wess, N. T. M. Hai, W. Reckien, T. Bredow, A. Fluegel, M. Arnold, D. Mayer, Hu. Keller, P. Broekmann, On the role of halides and thiols in additive-assisted copper electroplating, Electrochim. Acta 89 (2013) 537-548. https://doi.org/10.1016/j.electacta.2012.10.152

3-8. Y. Tsuru, M. Nomura, F.R. Foulkes, Effects of chloride, bromide and iodide ions on internal stress in films deposited during high speed nickel electroplating from a nickel sulfamate bath, J. Appl. Electrochem. 30 (2000) 231-238. https://doi.org/10.1023/A:1003970925918

3-9. W. C. Grande and J. B. Talbot, Electrodeposition of Thin Films of Nickel-Iron: II. Modeling, 140 (1993) 675. https://doi.org/10.1149/1.2056141

3-10. W. C. Grande and J. B. Talbot, Electrodeposition of Thin Films of Nickel-Iron: I . Experimental, J. Electrochem. Soc.140 (1993) 669. https://doi.org/10.1149/1.2056140

3-11. A. Karimzadeh, M. Aliofkhazraei, F. C. Walsh, A review of electrodeposited Ni-Co alloy and composite coatings: Microstructure, properties and applications, Surf. Coat. Technol. 372 (2019) 463-498. https://doi.org/10.1016/j.surfcoat.2019.04.079

3-12. N. Zech, E. J. Podlaha D. Landolt, Anomalous Codeposition of Iron Group Metals: I. Experimental Results, J. Electrochem. Soc. 146 (1999) 2886. https://doi.org/10.1149/1.1392024

3-13. M. Matlosz, Competitive Adsorption Effects in the Electrodeposition of Iron-Nickel Alloys, J. Electrochem. Soc. 140 (1993) 2272. https://doi.org/10.1149/1.2220807

3-14. A. Saraby-Reintjes, M. Fleischmann, Kinetics of electrodeposition of nickel from watts baths, Electrochimi. Acta 29 (1984) 557-566, https://doi.org/10.1016/0013-4686(84)87109-1

3-15. Y. -P. Lin, J. R. Selma, Electrodeposition of Corrosion-Resistant Ni-Zn Alloy: I . Cyclic Voltammetric Study, J. Electrochem. Soc. 140 (1993) 1299. https://doi.org/10.1149/1.2220974

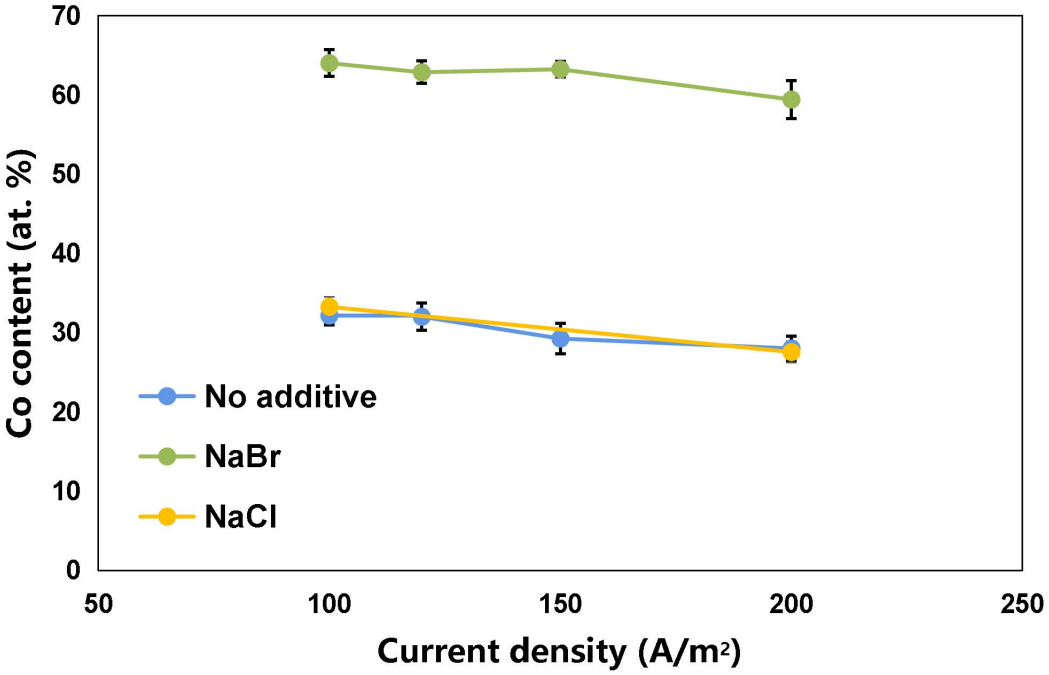

Fig. 3-1 Relationship between the Co content and the current density in electrodeposited Ni-Co alloys with different additives.

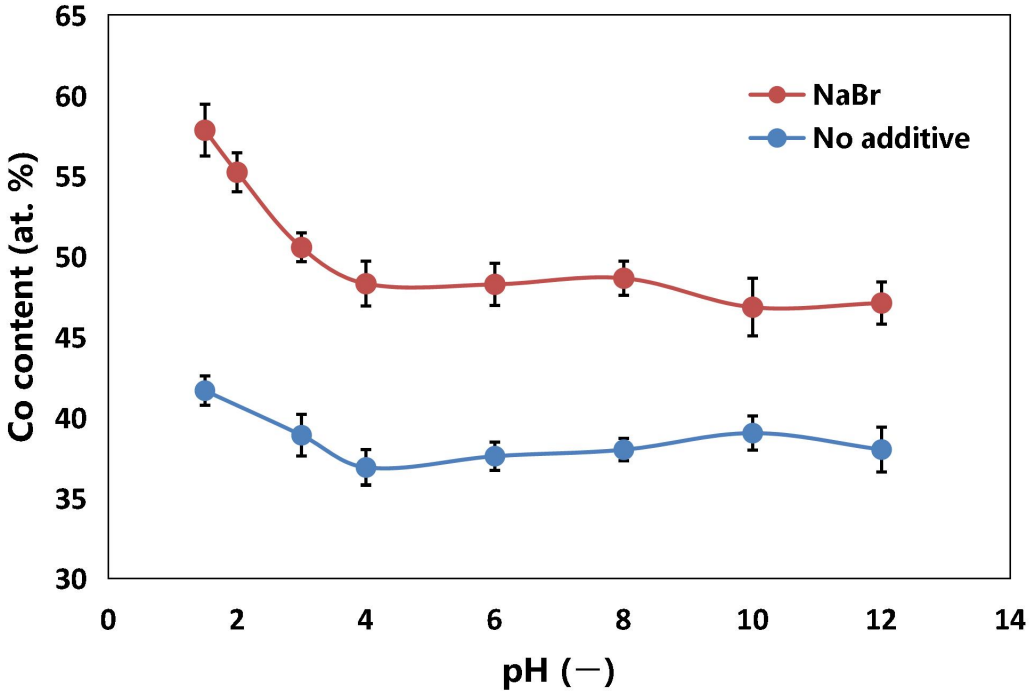

Fig. 3-2 Relationship between the Co content and pH value in Ni-Co electrodeposition with and without the addition of NaBr at the current density of 50 A/m^2.

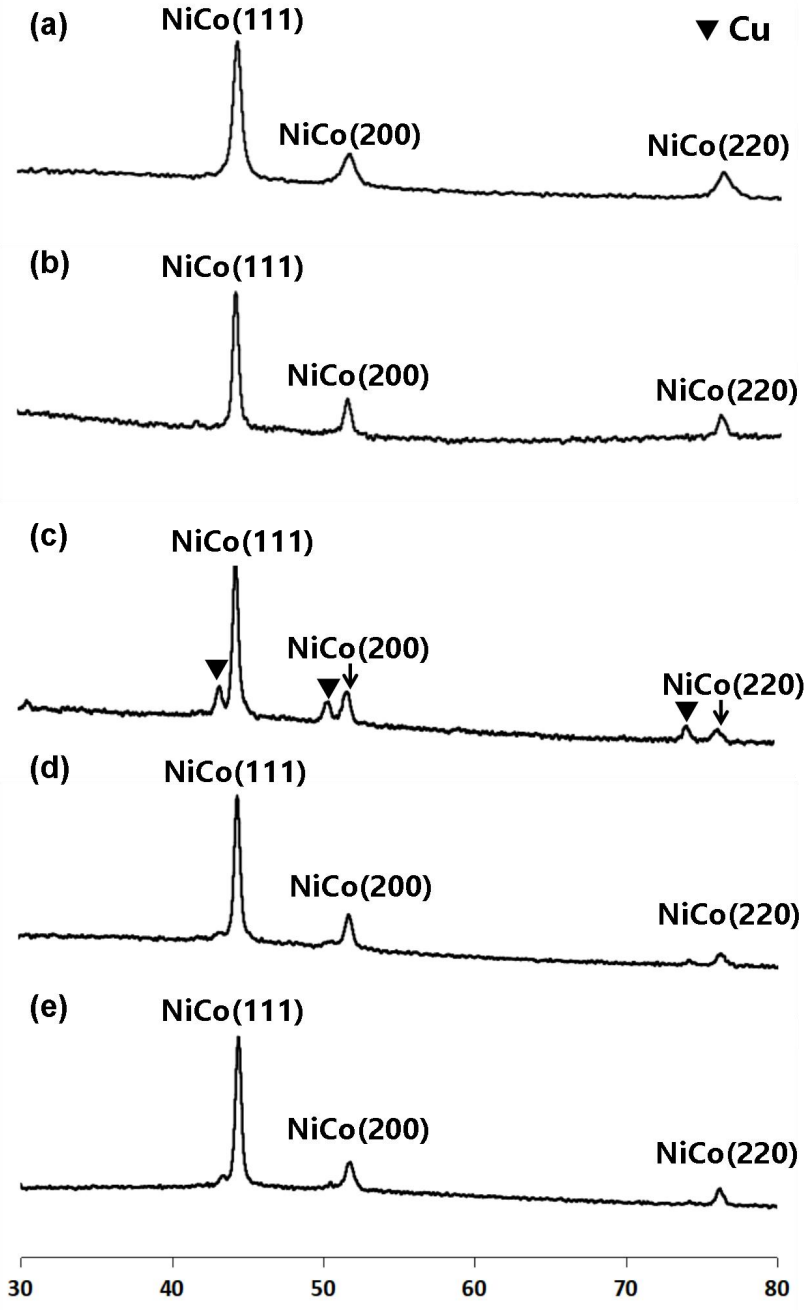

Fig. 3-3 XRD patterns of Ni-Co alloys electrodeposited at 200 A/m^2 with different additive conditions and at different pH: (a) NaBr, pH 1.5, (b) NaBr, pH 4, (c) no additive, pH 1.5, (d) no additive, pH 4, (e) no additive, pH 8.

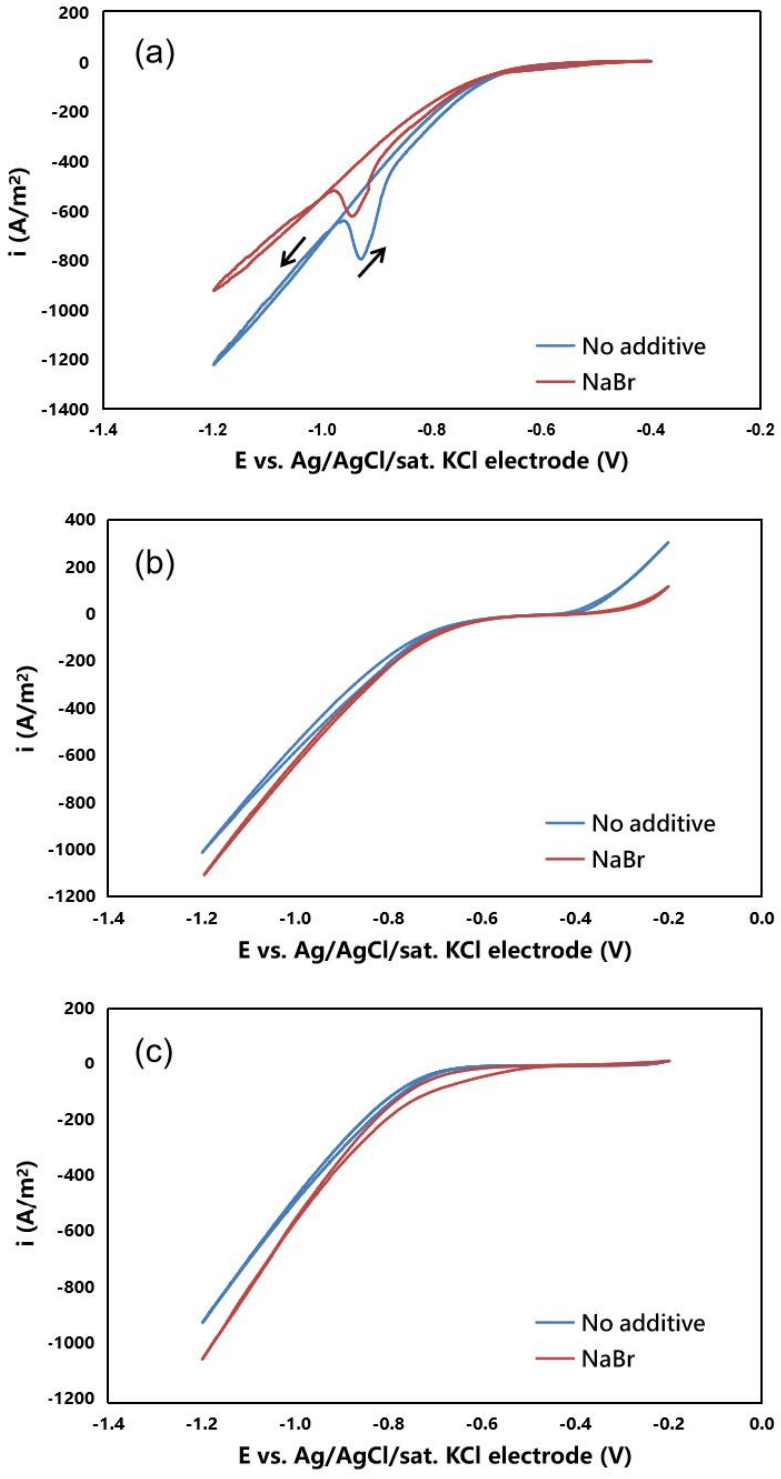

Fig. 3-4 Cyclic voltammograms of (a) Ni deposition, No. 1 and No. 4, (b) Co deposition, No. 2 and No. 5, (c) Ni-Co co-deposition, No. 3 and No. 6.

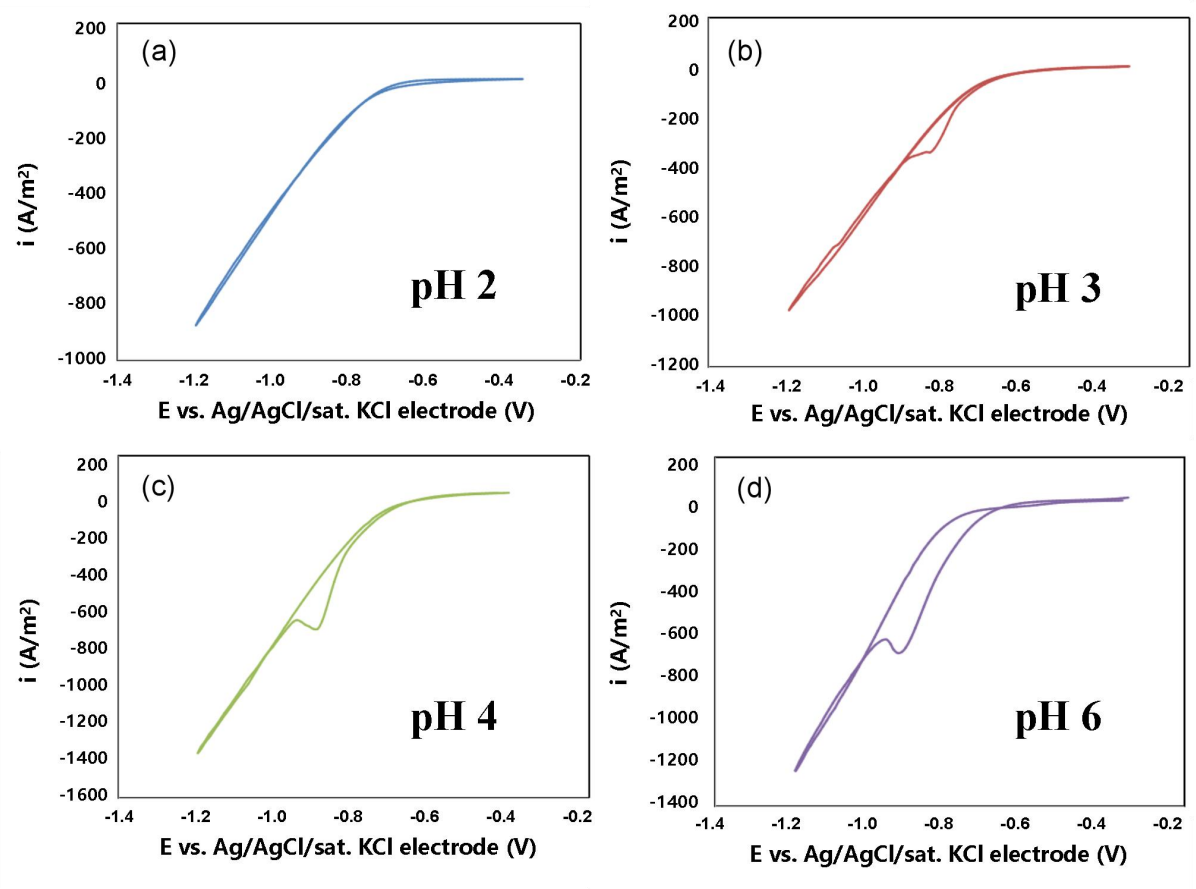

Fig. 3-5 Cyclic voltammograms of Ni electrodeposition at (a) pH 2, (b) pH 3, (c) pH 4 and (d) pH 6 without NaBr.

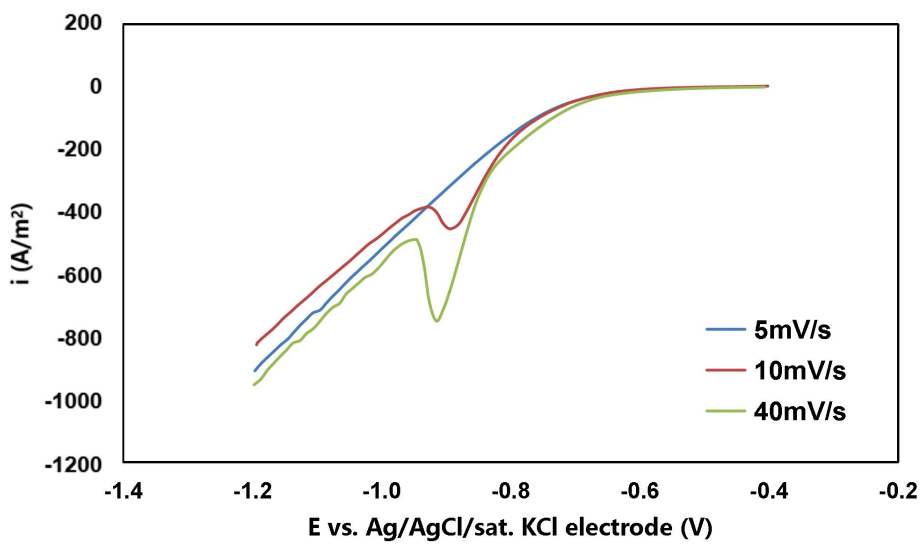

Fig. 3-6 Linear sweep voltammograms of Ni electrodeposition at different scan rates (positive sweep) without NaBr.

CHAPTER 4

Micro-Mechanical Characterization of Ni-Co Alloy Deposits

4-1. Introduction

In chapter 2, the mechanical property characterization of electrodeposited Ni-Co alloys were conducted by hardness test. However, mechanical properties of metallic materials are known to have a sample size effect [4-1~4-3], where an increase in the strength is observed as the size of the sample used in the mechanical property characterization reaches the micro-scale or smaller. Dimensions of the movable components in miniaturized electronic devices are often on the micro-scale or smaller. Hence, the sample size effect has to be considered in the mechanical property characterization.

Mechanical property can be easily measured by hardness test [4-4, 4-5]. The hardness is determined from the indentation mark created on the surfaces of the electrodeposited material after applying a constant loading for a length of time. Generally, a large indentation mark is generated on a soft electrodeposited material, and the indentation mark becomes small when the mechanical strength is high. From the size of the indentation mark and the loading force, the hardness can be calculated. The

hardness is called micro-hardness [4-4] or nano-hardness [4-5] when the indentation mark is on the micrometer or nanometer scale, respectively. In a study on micro-hardness of electrodeposited nickel-cobalt alloys [4-5], the micro-hardness is reported to be dependent on the current density used in the alloy electrodeposition, with the micro-hardness increasing along with increasing current density. However, materials surrounding the indentation mark, especially materials at the bottom of the indentation mark, could also affect generation of the indentation mark [4-6]. Therefore, it is difficult to include the sample size effect in the clarification of the mechanical properties on the micro-scale by a hardness test.

For precise evaluation of the mechanical property on the micro-scale toward micro-components in miniaturized electronic devices, micro-compression [4-7~4-9] micro-tensile [4-10], and micro-bending [4-11~4-13] tests are developed. Micro-mechanical properties of micro-grained nickel, nano-grained nickel [4-14], nano-grained copper [4-12], nano-grained gold, nano-grained gold-copper alloys, amorphous nickel-phosphorus alloy, and single crystalline nickel-cobalt alloys [4-15] are reported in previous studies. On the other hand, there is still very limited reporting on micro-mechanical properties of polycrystalline nickel-cobalt alloys.

Nickel-cobalt alloys applied in MEMS are prepared by alloy electrodeposition, and electrodeposited nickel-cobalt alloys are polycrystals. Mechanical properties of metals are closely related to their average grain size and the composition. The relationship between the average grain size and mechanical strength usually follows the Hall-Petch relationship, where the strength is inversely proportional to square root of the average grain size. Meanwhile, the strength is dependent on the composition (cobalt content) in

a nickel-cobalt alloy since the nickel-cobalt system forms a solid-solution that results in a strengthening effect. In addition, the average grain size and composition are easily affected by the electrodeposition conditions, such as the current density, the use of additives (surface brightener), and composition of the bath. This implies micro-mechanical properties of electrodeposited nickel-cobalt alloys are dependent on the electrodeposition condition.

In this work, nickel-cobalt alloys were electrodeposited from a sulfamate bath, and the mechanical properties on the micro-scale are evaluated by compression test using micro-pillar type specimens fabricated from the electrodeposited alloys by focused ion beam (FIB). Effects of the electrochemical parameters, such as the current density, on the average grain size and cobalt content are reported. Then, contributions of the grain boundary strengthening mechanism and solid-solution strengthening mechanism on the micro-mechanical properties are studied. The yield strength is determined from the engineering stress-engineering strain curve generated from the micro-compression test, and compared with the micro-hardness determined from micro-Vickers hardness test.

4-2. Experimental

Micro-pillar type specimens were fabricated from the nickel-cobalt alloys by a focused ion beam system (FIB, FB2100, Hitachi, Tokyo, Japan) using Ga as the liquid metal ion source. A four-step milling method using different beam currents was applied to produce micro-pillars with desired and precise dimensions. The beam currents were 6.64, 1.48 and 0.35 nA for coarse milling and 0.07 nA for fine milling and final polishing. The micro-pillar had a cuboidal shape with dimensions of 20 μm in height and a 10 × 10 μm^2 square cross-section. Observations of the micro-pillars were

conducted through a scanning ion microscope (SIM) installed in the FIB before and after the micro-compression test.

The micro-compression test was conducted using a test machine specially designed for micro-sized samples. The test machine was equipped with a flat-topped indenter with a diameter of 50 μm on the top surface. The test machine had the load resolution of 10 μN, and the displacement resolution was 5 nm. A constant displacement rate of 0.1 μm/s was used in all micro-compression tests, which gave a constant strain rate at 5×10^{-3} s^{-1}. More details of the test machine are reported in a previous study

4-3. Micro-mechanical property

SIM images of micro-pillars fabricated from the alloys are shown in Fig. 4. The micro-pillars were all precisely fabricated with a square cross-section, and the aspect ratio of height to length of one side was two. Boundaries of the crystal structure in metallic materials could be observed from the SIM images. On the surfaces of the micro-pillars prepared in this study, camouflage patterns were observed, and these were suggested to be the texture boundaries since the sizes of the patterns were all much larger than the average grain size values estimated from the Scherrer equation. For instance, the average grain size of the alloy electrodeposited at 15 mA/cm^2 in the sulfamate bath containing the nickel bromide was 21.6 nm, and the average size of the camouflage patterns was in the hundreds of nanometer level.

Images of the micro-pillars after the micro-compression test are shown in Fig. 5. All micro-pillars showed swelling at some parts of the cross-section after the compression, which is a typical deformation behavior of nanocrystalline metallic materials. Engineering stress-engineering strain (SS) curves generated from

compression tests of the micro-pillars are shown in Fig. 6. The yield point was not clear in all SS curves. Therefore, the yield strength (σ_y) was determined from the 0.2% offset line of the elastic deformation region [4-16]. A summary of the yield strengths is listed in Table 2. The yield strengths obtained in this study were all higher than bulk electrodeposited nickel-cobalt alloys reported by Li et al. (1200 MPa) [37], and 2~3 folds of the values reported for nickel-ferrum alloys (700 MPa) [4-17].

Relationships between the average grain size, micro-hardness and yield strength are shown in Fig. 7. Generally, for both of the micro-hardness and yield strength, strengthening was observed following a refinement of the average grain size as illustrated by the dashed trendlines. This trend followed the Hall-Petch relationship well [30, 31], and confirmed that the mechanical strength was mostly dependent on the grain boundary strengthening mechanism. Alloys with smaller grain size have less dislocations pile up and less stress at grain boundaries, which contributes to a higher mechanical strength. The highest yield strength at 2.37 GPa was obtained from the micro-pillar having the average grain size at 13.6 nm and 58.48 at.% of cobalt, and the highest micro-hardness at 457.4 HV was also obtained from the alloy with the same average grain size and composition. The alloy having the finest average grain size at 13.2 nm had a micro-hardness of 438.8 HV and a yield strength of 2.18 GPa, which both values were the second highest among the alloys/micro-pillars evaluated in this study. This result indicated that the composition, via the solid-solution strengthening mechanism, also had a significant contribution to the overall strength since the cobalt content in the alloy with the average grain size at 13.2 nm (32.78 at.%) was much lower than that of the alloy made of 13.6 nm grains (58.48 at.%).

Relationships between the composition, micro-hardness and yield strength are shown in Fig. 8. The composition dependency of the mechanical strength was not that obvious. A weak relationship between the composition and the strength could be concluded since a local maximum in the strength was obtained as the composition approached roughly 58 at.% of cobalt. For the three alloys electrodeposited with the two additives (nickel bromide and the Surf-Bright, ■), the average grain size merely changed between 13.6 and 13.9 nm and the cobalt content varied between 58.48 to 66.64 at.% when the current density changed from 12 to 20 mA/cm^2. In these three alloys, a decrease in both of the micro-hardness and yield strength was observed following an increase in the cobalt content as indicated by the dashed trendlines in Fig. 8.

Information of the Tabor factor [4-18], which is the ratio of the micro-hardness in the unit of MPa by the yield strength also in the unit of MPa (H_v in MPa/σ_y in MPa), is provided in Table 2. The Tabor factor is reported to be between 3 and 4 in literature [4-18]. In this study, the Tabor factors were between ca. 1.9 and 2.2. Fig. 9 shows a plotting of the Tabor factor against the yield strength, and a linear relationship (R^2 value = 0.88) between the two could be observed. Generally, the Tabor factor became smaller along with an increase in the yield strength.

4-4. Chapter Summary

The nickel-cobalt alloys were prepared by alloy electrodeposition with a sulfamate bath. Micro-compression test was conducted using micro-pillar type specimens to investigate the mechanical strength on the micro-scale. The yield strength was found to be highly dependent on the average grain size based on the grain boundary strengthening mechanism.

References

4-1. M. D. Uchic, D. M. Dimiduk, J. N. Florando, W. D. Nix, Sample Dimensions Influence Strength and Crystal Plasticity, Science 305 (2004) 986-989. https://doi.org/10.1126/science.1098993.

4-2. J. R. Greer, W. C. Oliver, W. D. Nix, Size dependence of mechanical properties of gold at the micron scale in the absence of strain gradients, Acta Mater. 53 (2005) 1821-1830. https://doi.org/10.1016/j.actamat.2004.12.031.

4-3. E. Valova, S. Armyanov, A. Franquet, K. Petrov, D. Kovacheva, J. Dille, J.-L. Delplancke, A. Hubin, O. Steenhaut, J. Vereecken, Comparison of the Structure and Chemical Composition of Crystalline and Amorphous Electroless Ni-W-P Coatings, J. Electrochem. Soc. 151 (2004) C385-C391. https://doi.org/10.1149/1.1705661.

4-4. I. Manika, J. Maniks, Effect of substrate hardness and film structure on indentation depth criteria for film hardness testing, J. Phys. D: Appl. Phys. 41 (2008) 074010. https://doi.org/10.1088/0022-3727/41/7/074010.

4-5. H. Tang, T. F. M. Chang, Y. W. Chai, C. Y. Chen, T. Nagoshi, D. Yamane, H. Ito, K. Machida, K. Masu, M. Sone, Au-Cu Alloys Prepared by Pulse Electrodeposition toward Applications as Movable Micro-Components in Electronic Devices, J. Electrochem. Soc. 165 (2018) D58-D63. https://doi.org/10.1149/2.0441802jes.

4-6. T. Hotta, T. F. M. Chang, C. Y. Chen, H. Sawae, Y. Imada, M. Mizoguchi, O. Kudo, R. Maeda, M. Sone, The Electrochemical Society, Micro-Compression Characterization and Thermal Stability of Electrolessly Plated Nickel Phosphorus Alloy, ECS J. Solid State Sci. Technol. 10 (2021) 035007. https://doi.org/10.1149/2162-8777/abedd3.

4-7. Y. Kihara, T. Nagoshi, T. F. M. Chang, H. Hosoda, T. Sato, M. Sone, Tensile behavior of micro-sized specimen fabricated from nanocrystalline nickel film, Microelectron. Eng. 141 (2015)17-20. https://doi.org/10.1016/j.mee.2015.01.001.

4-8. K. Asano, H. Tang, C.Y. Chen, T. Nagoshi, T. F. M. Chang, D. Yamane, T. Konishi, K. Machida, K. Masu, M. Sone, Microelectronic Engineering Promoted bending strength in micro-cantilevers composed of nanograined gold toward MEMS applications, Microelectron. Eng. 196 (2018) 20-24. https://doi.org/10.1016/j.mee.2018.04.021

4-9. K. Suzuki, T. F. M. Chang, K. Hashigata, K. Asano, C. Y. Chen, T. Nagoshi, D. Yamane, H. Ito, K. Machida, K. Masu, M. Sone, Sample geometry effect on mechanical property of gold micro-cantilevers by micro-bending test, MRS Comm. 10 (2020) 434-438. https://doi.org/10.1557/mrc.2020.38.

4-10. H. Imamura, T. Nagoshi, A. Yoshida, T. F. M. Chang, S. Onaka, M. Sone, Evaluation of anisotropic structure in electrodeposited Ni film using micro-sized cantilever. Microelectron. Eng. 100, (2012) 25-27. https://doi.org/10.1016/j.mee.2012.07.118.

4-11. Y. Xiao, B. Gan, A. S.Sologubenko, R. Spolenak, J. M.Wheeler, Size- and strain rate-dependence of nickel and Ni-Co micropillars with varying stacking fault energy, Mater. Sci. Eng. A 800 (2021) 140266. https://doi.org/10.1016/j.msea.2020.140266.

4-12. S. Goldbach, R. de Kermadec, F. Lapicque, Electrodeposition of Ni-Co alloys from sulfamate baths, J. Appl. Electrochem. 30 (2000) 277-284.

4-13. A. Bai, C. C. Hu, Effects of electroplating variables on the composition and morphology of nickel-cobalt deposits plated through means of cyclic voltammetry,

Electrochim. Acta 47 (2002) 3447-3456. https://doi.org/10.1016/S0013-4686(02)00281-5.

4-14. K. Takashima, Y. Higo, S. Sugiura, M. Shimojo, Fatigue crack growth behavior of micro-sized specimens prepared from an electroless plated Ni-P amorphous alloy thin film, Mater. Trans. 42 (2001) 68-73. https://doi.org/10.2320/matertrans.42.68.

4-15. W. F. Hosford, Mechanical Behavior of Materials, 2nd edition, Cambridge University Press, New York, 2010.

4-16. Z. Zhong, Y. Gu, Y. Yuan, Microstructural stability and mechanical properties of a newly developed Ni-Fe-base superalloy, Mater. Sci. Eng. A. 622, (2015) 101-107. https://doi.org/10.1016/j.msea.2014.11.010.

4-17. Y. Li, H. Jiang, W. Huang, H. Tian, Effects of peak current density on the mechanical properties of nanocrystalline Ni-Co alloys produced by pulse electrodeposition, Appl. Surf. Sci. 254 (2008) 6865-6869. https://doi.org/10.1016/j.apsusc.2008.04.087.

4-18. D. Tabor, The hardness of solids, Rev. Phys. Tech. 1 (1970) 145.

	Current density (mA/cm^2)	Grain size (nm)	Co content (at. %)	Micro-hardness, H_v (HV)
Sulfamate bath only	15	21.2	21.5	364.0 ± 11.7
Sulfamate bath + Nickel bromide	12	20.1	59.58	422.0 ± 11.7
	15	21.6	60.05	376.2 ± 14.4
	18	28.2	57.39	395.6 ± 17.8
	20	20.9	58.40	414.0 ± 12.4
Sulfamate bath + Surf-Bright	15	13.2	32.78	438.8 ± 9.2
Sulfamate bath + Nickel bromide + Surf-Bright	12	13.6	65.47	426.2 ± 13.5
	15	13.9	66.64	417.2 ± 11.0
	20	13.6	58.48	457.4 ± 14.5

Table. 4-1 Effects of the current density on the average grain size, cobalt content and micro-hardness.

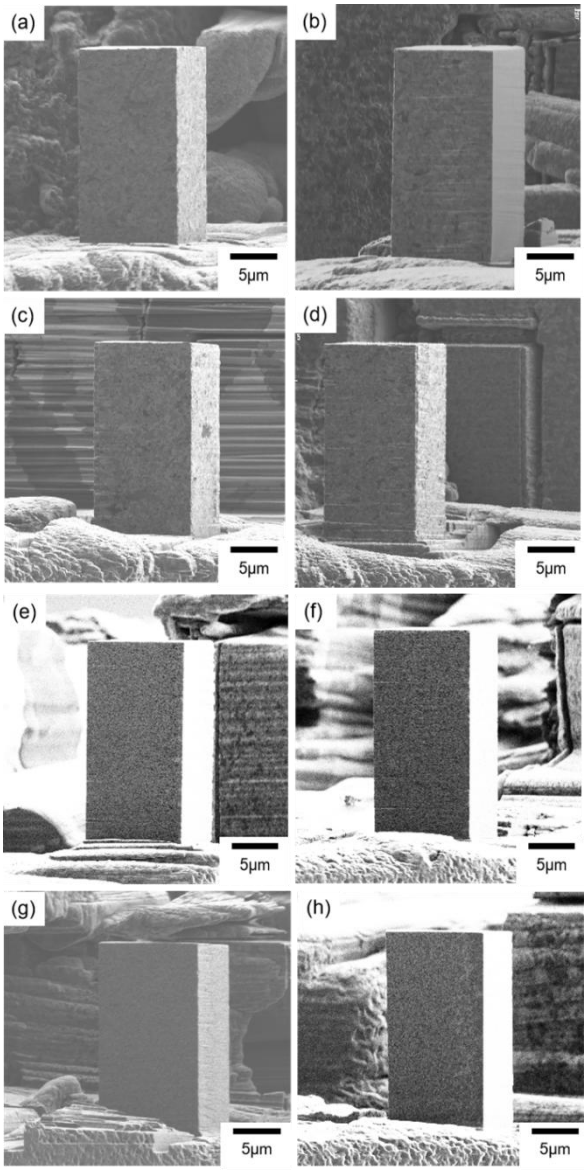

Fig. 4-1 SIM images of the micro-pillars fabricated from the nickel-cobalt alloys electrodeposited with the bath containing (a)~(d) nickel bromide, (e) the Surf-Bright, or (f)~(h) both nickel bromide and the Surf-Bright, and at a current density of (a) and (f) 12 mA/cm^2, (b), (e) and (g) 15 mA/cm^2, (c) 18 mA/cm^2 and (d) and (h) 20 mA/cm^2.

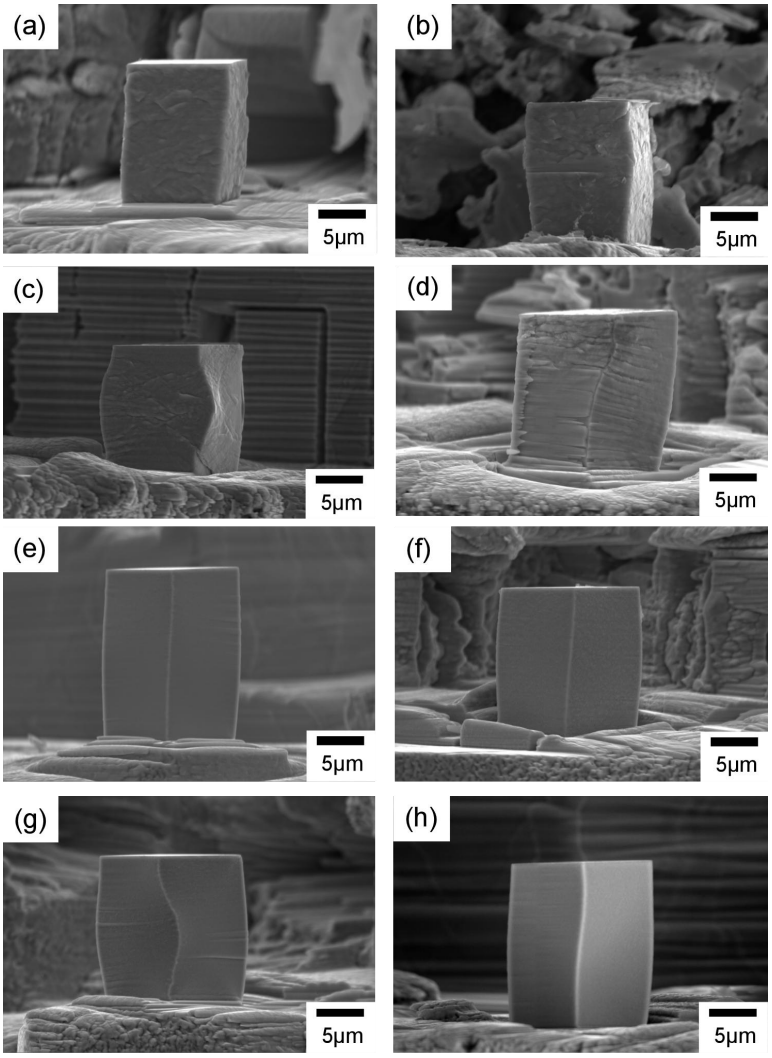

Fig. 4-2 SEM image of the deformed micro-pillars fabricated from the nickel-cobalt alloys electrodeposited with the bath containing (a) ~ (d) nickel bromide, (e) the Surf-Bright, or (f) ~ (h) both nickel bromide and the Surf-Bright, and at a current density of (a) and (f) 12 mA/cm^2, (b), (e) and (g) 15 mA/cm^2, (c) 18 mA/cm^2 and (d) and (h) 20 mA/cm^2.

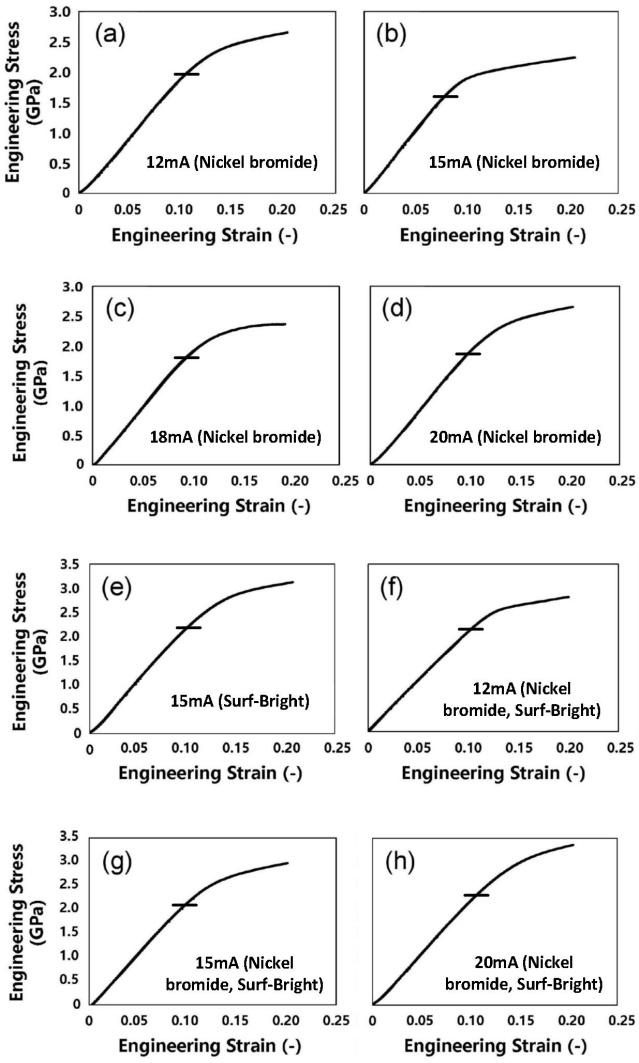

Fig. 4-3 Engineering stress-strain curves generated from compression of the micro-pillars fabricated from the nickel-cobalt alloys electrodeposited with the bath containing (a)~(d) nickel bromide, (e) the Surf-Bright, or (f)~(h) both nickel bromide and the Surf-Bright, and at a current density of (a) and (f) 12 mA/cm^2, (b), (e) and (g) 15 mA/cm^2, (c) 18 mA/cm^2 and (d) and (h) 20 mA/cm^2.

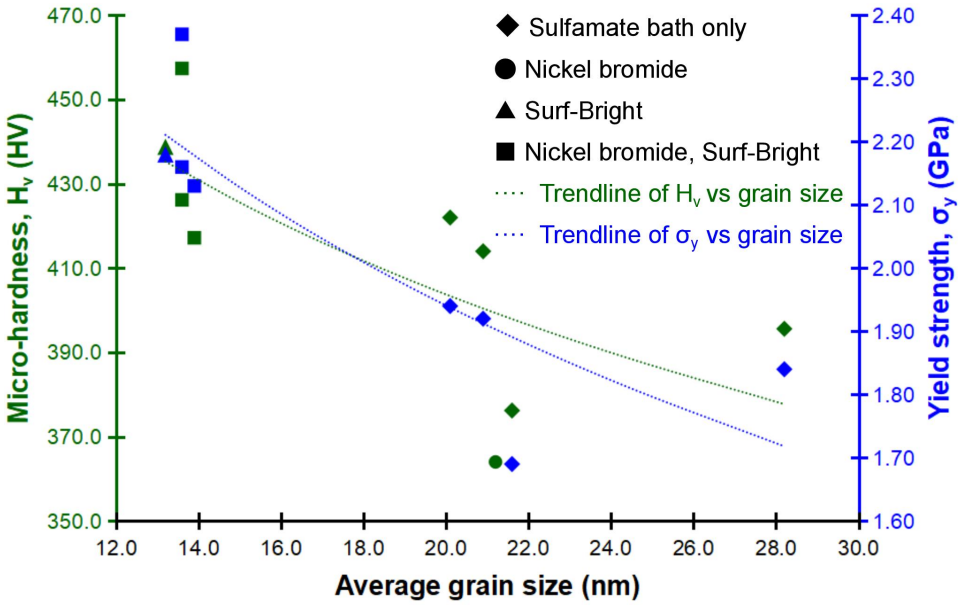

Fig. 4-4 Relationships between the average grain size, micro-hardness and yield strength.

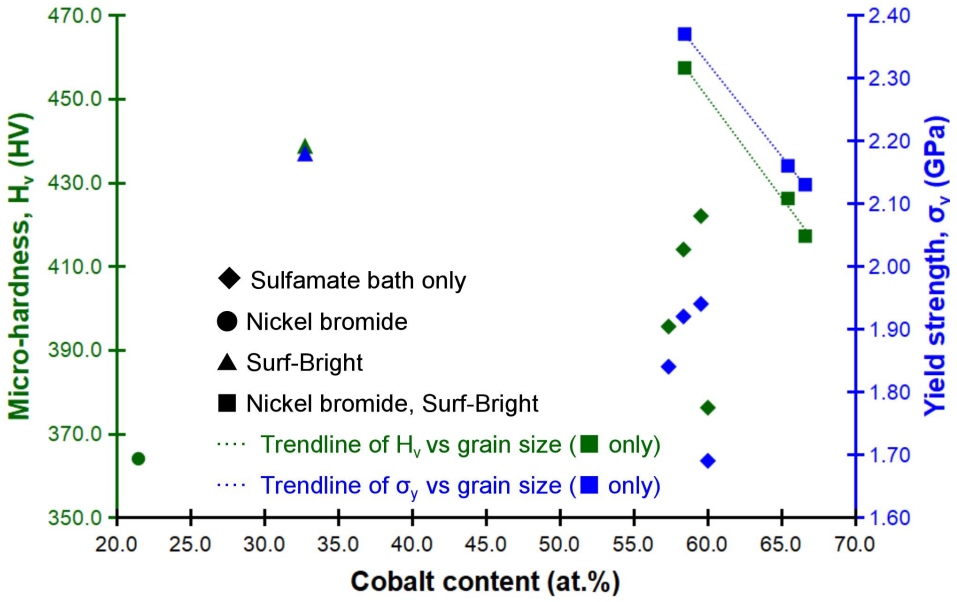

Fig. 4-5 Relationships between the composition, micro-hardness and yield strength.

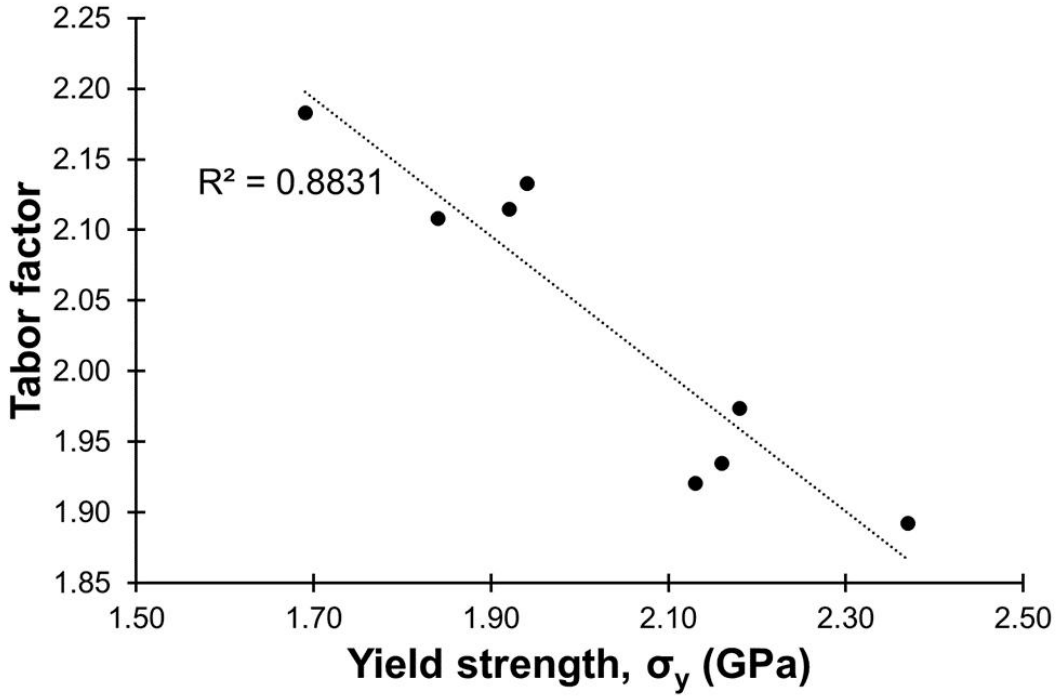

Fig. 4-6 Relationship between the yield strength and the Tabor factor.

CHAPTER 5

Electrodeposition and Micro-Mechanical Characterization of Ni-B Alloys

5-1. Introduction

Miniaturized electronic devices are becoming more complex and smaller to fulfill requirements in future trends of electronics industry, such as sizes of the movable component in microelectromechanical systems (MEMS) are often on the micro-scale or nano-scale [5-1], and the high-density packaging of semiconductor devices is increasingly demanded. Ni and its alloy electrodeposits have been widely applied in miniaturized electronics due to their corrosion resistance, electrocatalytic activity, excellent magnetic and mechanical properties [5-2, 5-3]. On the other hand, electrodeposited Ni-based materials typically exhibit low thermal stability and lose their high mechanical strengths after annealing at a relatively low temperature [5-4], which is a major limitation in their applications. For example, the abnormal grain growth of electrodeposited Ni can be observed after heat treatment of 200 °C for 2 h [5-5].

Incorporation of B is an effective method to enhance the mechanical strength, wear resistance and thermal characteristic of Ni-based materials [5-6~5-8]. The formation of intermetallic compounds, such as Ni_3B or Ni_2B, contributes to outstanding mechanical

performance by the precipitation strengthening mechanism in Ni-B plating. For instance, Ni-B alloys are regarded as potential electrical contact materials in electronic and semiconductor industries due to their electrical conductivity, erosion resistance and solderability [5-9, 5-10]. It is also reported that Ni-B alloys have a better performance in the under bump metallization (UBM) packaging process comparing to Ni-P [5-11]. In addition, Kwon et al. have reported Ni-B MEMS-based micro-probe for wafer-level integrated circuit tests with a higher stiffness than conventional Ni-Co probe [5-12].

Furthermore, heat treatment or thermal annealing is a common process applied in fabrication of electronic components, such as the fabrication of MEMS accelerometer [5-13]. Mechanical properties of electrodeposits are expected to be affected by the heat treatment process. For electrodeposited Ni-B alloys, after the heat treatment, Ni3B intermetallic phase is formed in the heat treated Ni-B alloys as reported in several works [5-14~516], and the Ni_3B phase leads to an increase in the hardness due to the precipitation strengthening mechanism [5-9]. The Ni-B alloys are also reported to soften when the heat treatment time is prolonged, or when a high heat treatment temperature is used [5-14, 5-16].

Electroless deposition and electrodeposition and physical vapour deposition techniques (e.g. sputtering) are common methods applied in fabrication of Ni-B alloy films [5-17]. On the other hand, physical vapour deposition methods are known to involve complex processing sequence and high process cost. Electroless deposition and electrodeposition methods are easily adoptable for production of electronic components because of the low production cost and simple process. Among the two deposition methods, electrodeposition offers a higher deposition rate, better crystallinity, higher

stability of the electrolyte and more uniform distribution of the second element in the metal matrix when comparing with the electroless deposition method. For instance, the deposition rate in electrodeposition is reported to be up to 600 times higher than the deposition rate in electroless deposition [5-18]. In addition, the composition and micro-structure in the deposited alloy can be easily controlled by the electrodeposition parameters, such as the current density and the use of additives [5-19]. Ni-B alloy deposition through an electroless method also suffers from a low bath life.

Mechanical properties of metallic materials often exhibit the sample size effect, which the mechanical strength varies as the size of the sample reduces to the micro-scale or smaller. Thus, the sample size effect has to be considered in the mechanical property evaluation for design of micro-components in miniaturized devices. Mechanical properties of electrodeposits can be evaluated by micro-hardness test [5-9, 5-10, 5-20]. Although the size of the indentation mark generated in a micro-hardness test could be on the micro-scale or smaller, the formation of the indentation mark is still affected by the substrate. In order to evaluate the mechanical property for the design of micro-components, mechanical test using specimens having the size on the micro-scale are developed [5-21].

In this study, mechanical properties on the micro-scale of electrodeposited Ni-B alloy films are characterized by micro-compression test using micro-pillar type specimens fabricated by a focused ion beam system. The mechanical strength and deformation behavior are determined by the micro-compression test. Results obtained from a micro-Vickers hardness tester are also prepared as comparisons. In addition,

effects of the heat treatment on the crystalline structure and mechanical properties of the electrodeposited Ni-B alloy films are evaluated to clarify the thermal stability.

5-2. Experimental

Cu plates (Kikuya PM Co., Ltd., Tokyo, Japan) in sizes of 10 mm × 10 mm were used as the substrates in the Ni-B alloy electrodeposition. The counter electrode was a Pt plate (Kikuya PM Co., Ltd., Tokyo, Japan). The electrodeposition was conducted at 50 ℃ with an additive-free Watt's bath (Okuno Chemical Industries Co. Ltd, Japan) containing 300 g/L $NiSO_4 \cdot 6H_2O$, 50 g/L $NiCl_2 \cdot 6H_2O$, and 50 g/L H_3BO_3. 10.0 vol.% EB-MK (dimethylamine borane as main ingredient), which is a commercially available additive provided by World Metal Co., Ltd., Osaka, Japan, was used as the boron source. The electrodeposition was conducted by a galvanostatic method with the current density ranged from 1 A/dm2 to 4 A/dm2, and continuous mixing of the bath was performed by stirring with a magnetic stirrer at 200 rpm. The thicknesses of Ni-B alloy films prepared in this study were all thicker than 50 μm, which was confirmed through observation of the cross-section.

The electrodeposited Ni-B alloy films were firstly heat treated under vacuum atmosphere (< 0.1 Pa) at different temperatures by a vacuum furnace (FT-01VAC-30, FULL-TECH Co., Ltd., Osaka, Japan), and an optimized heat treat temperature was set at 250 °C. The microhardness test results are provided in the supplementary (Fig. S1). Then, more alloy films were heat treated at 250 °C for 1 h, 2 h and 4 h. The surface morphology of the films was observed by a scanning electron microscope (SEM, SU4300SE Hitachi, Ltd., Tokyo, Japan). The surface roughness (Ra) was characterized by a laser scanning microscope (VK-X3000, Keyence Corp., Osaka, Japan). Crystalline

characteristics of the Ni-B alloy films were characterized by an X-ray diffractometer (XRD, Ultima IV, Rigaku Corp., Tokyo, Japan). The Ni and B contents were determined by inductively coupled plasma mass spectrometry (ICPS-8100, Shimadzu Corp., Kyoto, Japan). Micro-hardness of the alloy films was evaluated by a micro-Vickers hardness tester (HMV-G20S, Shimadzu Corporation, Kyoto, Japan) at a loading of 200 g.

The micro-pillar type specimens were fabricated from the Ni-B alloy films with a focused ion beam system (FIB, FB2100, Hitachi, Ltd., Tokyo, Japan). Each micro-pillar had a hexahedron shape with a dimension of an 8 μm × 8 μm square cross-section and 16 μm in height. Observations of the as-fabricated and deformed micro-pillars were conducted through a scanning ion microscope (SIM) equipped in the FIB system and the SEM. The micro-compression test was conducted using a test machine specially designed for micro-sized specimens [5-22]. The test machine system was equipped with a flat-topped indenter having a diameter of 50 μm on the tip surface. The displacement rate was kept at a constant speed of 0.1 μm/s in all micro-compression tests.

5-3. Surface morphology

SEM images of the as-deposited and heat-treated Ni-B alloy films are shown in Fig. 1. The as-deposited alloy film had a uniform surface as shown in Fig. 1(a), while a few particles were observed in the 250 °C and 2 h heat-treated film as shown in Fig. 1(b). Furthermore, the average size of the particles was found to increase after 250 °C and 4 h of the heat treatment (Fig. 1(c)). The particles are suggested to be the intermetallic compound, Ni_3B.

Values of the surface roughness (Ra) of the as-deposited alloy films are summarized in Fig. 2. The surface roughness significantly decreased as the current density increased, and the surface roughness reached 0.16 μm when 4 A/dm^2 was used. One explanation for the reduced surface roughness is that the nucleation rate becomes higher along with an increase in the current density in electrodeposition, and an increased nucleation rate often leads to a more uniform surface morphology.

5-4. Composition

The B content in the electrodeposited Ni-B alloy films was confirmed to decrease as the current density increased as shown in Fig. 3. Ogihara et al. reported a similar tendency [5-23], which the B content decreased following an increase in the current density. It is suggested that the deposition rate of Ni is enhanced when a higher current density is used, while the deposition rate of B remains almost the same as the current density varies. In this way, the B content is lowered when a higher current density is used.

In this study, three of the Ni-B alloys fabricated at current densities of 1 A/dm^2, 1.5 A/dm^2 and 4 A/dm^2 (B content of 14.3 at.%, 7.1 at.% and 2.8 at.%) were selected for the heat treatment at 250 °C. Based on the phase diagram of Ni-B [5-24], most B in the heat-treated Ni-B alloys prepared in this study would exist as an intermetallic compound, Ni_3B, within this B content range, and only a few B atoms can form solid solution in Ni matrix. The Ni_3B is expected to work as precipitates in the alloy film and affects mechanical properties of the Ni-B alloy films.

5-5. Crystalline characterization

XRD characterization was conducted to examine effects of the heat treatment on the crystalline structure in the electrodeposited Ni-B alloy films. The XRD patterns are shown in Fig. 4. The major diffraction peaks of the Ni matrix were sharpened after the 250 °C heat treatment, and this suggested an improvement in the crystallinity. Besides, after heat treatment at 250 °C for 4 h, some new diffraction peaks were observed and believed to be contributed by the intermetallic compound, Ni3B. This crystal structural change is reported in other studies.

The mean size of the ordered domains (L) in crystallography can be estimated by the Scherrer equation:

$$L = \frac{K\lambda}{\beta \cos\theta}$$

where K is a shape factor, λ is the wave length of the X-ray, β is the width at half maximum intensity, and θ is the Bragg angle. The value of L is commonly treated as the average grain size of a material. In this study, the value of L could be regarded as the average grain size of the Ni-rich matrix.

A slight increase in L was observed along with an increase in the current density as shown in Fig. 5. This increase in L implies an improvement in the crystallinity. As mentioned in previous section, the B content decreased from 14.3 at.% to 2.8 at.% as the current density increased form 1 A/dm2 to 4 A/dm2. Hence, the increase in L is suggested to be a result of the decreased B content [5-25]. A more significant increase in L was observed in the 1 h heat treated electrodeposits, indicating a positive influence on the crystallinity of the Ni-rich matrix by the heat treatment. Also, L was hardly

affected when prolonging the heat treatment time to 2 h. In addition, the growth of (220) oriented Ni (near 2θ = 77°) was confirmed.

5-6. Hardness and micro-compression characteristics

SEM images of the micro-pillars after the micro-compression test are shown in Fig. 6. Images of the micro-pillars before the micro-compression test are provided in the supplementary (Fig. S2). All micro-pillars fabricated from the as-deposited Ni-B films (non-heat treated) showed a typical ductile deformation behavior. The deformation behavior changed to brittle fractures after the 250 °C heat treatment. The ductile-to-brittle transition was observed in the Ni-B alloy micro-pillar fabricated at a current density of 1 A/dm^2 when the heat treatment time was shorter than 1 h. The transition occurred in the micro-pillars fabricated at 1.5 A/dm^2 and 4 A/dm^2 with a longer heat treatment time at 2 h and 4 h, respectively. This transition in the deformation behavior is believed to be related to the B content and the precipitation of Ni_3B. The precipitation of Ni_3B caused a significant increase in the flow stress, and the shear band propagation became more likely to occur and the micro-pillar deformed through a brittle fracture type catastrophic failure. The precipitation of Ni_3B is expected to occur at a higher rate in Ni-B alloy films with a higher B content, thus, the transition occurs in a shorter period of the heat treatment time.

Engineering stress-engineering strain curves generated from the micro-compression test are shown in Fig. 7. More engineering stress-engineering strain curves are provided in Fig. S3. For the micro-pillar that showed a ductile deformation, the yield point was not clear in the engineering stress-engineering strain curve. Thus,

the yield point was determined by the 0.2 % offset line of the elastic deformation region and used as the compressive strength. The 2 h heat treated Ni-B alloy film deposited at 1 A/dm^2 (14.3 at.% B) showed the maximum yield strength of 5.05 GPa among all ductile micro-pillars. For the brittle micro-pillar, the fracture strength was used as the compressive strength. A maximum compressive strength of 5.52 GPa was confirmed in a Ni-B alloy micro-pillar deposited at 4 A/dm^2 (2.8 at.% B) after 4 h of the heat treatment. Generally, the Ni-B alloy micro-pillar with a high B content showed a high mechanical strength, and further strengthening was observed after the heat treatment.

For the as-deposited (non-heat-treated) Ni-B alloy films, relationships between the B content, micro-hardness and yield strength are plotted in Fig. 8. Dependence of the hardness and yield strength on the B content were similar. The hardness and yield strength of the Ni-2.8%B alloy film was greatly attributed to the solid solution strengthening mechanism. As the B content increased from 2.8 at.% to 7.1 at.%, it is suggested that the decrease in the volume fraction of the nanocrystalline Ni phase caused a slight softening effect. The high mechanical strength of Ni-14.3%B alloy is considered to be a result of high Ni_3B content. Relationships between the compressive strength and L are shown in Fig. 9. Improvement of the crystallinity was observed after the 250 °C heat treatment. In the 1 h and 2 h heat treated alloys, a decrease in the strength was observed along with an increase in L, which can be explained by the Hall-Petch effect. Regarding effects of the heat treatment on the mechanical properties, a slight decrease in the compressive strength was observed after 1 h of the heat treatment (●→▲) in the three Ni-B alloy films. The mechanical strength was lowered because of the residual stress relaxation, which often leads to a decrease in the

mechanical strength. In the meantime, the amount of Ni_3B in the Ni-B alloy films might be still low because of the limited heat treatment time and resulted insignificant influences on the overall strength. On the other hand, a significant strengthening effect was observed when the heat treatment time was longer than 2 h (▲→◆/■), while L remained at the same level. Hence, it is believed that the continuing precipitation of Ni_3B resulted this strengthening effect in the Ni-B alloys by the precipitation strengthening mechanism.

5-7. Chapter Summary

Ni-B alloy films with the B content ranged from 2.8 at.% to 14.3 at.% were electrodeposited by controlling the current density. The B content was found to decrease along with an increase in the current density. Surface roughness (Ra) of the alloy films decreased following with an increase in the current density. Micro-compression test was conducted to appraise the micro-mechanical strength. As-deposited Ni-B alloy films showed high yield strengths in a range of 4 GPa to 5 GPa and ductile deformation behaviors. The high strength was further enhanced after the 250 °C heat treatment for 1 h to 4 h, and a maximum fracture strength of 5.52 GPa was obtained owing to the precipitation strengthening effect by the intermetallic compound, Ni3B. Along with an increase in the heat treatment time, the deformation behavior changed from ductile to brittle. In conclusion, the electrodeposited Ni-B alloy films showed an excellent micro-mechanical strength and thermal stability and demonstrated the applicability toward miniaturized electronics.

Reference

5-1. T. Konishi, D. Yamane, T. Matsushima, G. Motohashi, K. Kagaya, H. Ito, N. Ishihara, H. Toshiyoshi, K. Machida, K. Masu, Novel Sensor Structure and Its Evaluation for Integrated Complementary Metal Oxide Semiconductor Microelectromechanical Systems Accelerometer, Jpn. J. Appl. Phys. 52 (2013) 06GL04. https://doi.org/10.7567/JJAP.52.06GL04.

5-2. C.-Y. Lee, W.-T. Mao, M.-D. Ger, H.-B. Lee, A study on the corrosion and wear behavior of nanocrystalline Ni single bond Mo electrodeposited coatings, Surf. Coat. Technol. 366 (2019) 286-295. https://doi.org/10.1016/j.surfcoat.2019.03.048.

5-3. Gh. B. Darbanda, N. Lotfi, A. Aliabadi, S. Hyun, S. Shanmugam, Hydrazine-assisted electrochemical hydrogen production by efficient and self-supported electrodeposited Ni-Cu-P@Ni-Cu nano-micro dendrite catalyst, Electrochim. Acta, 382 (2021) 138335. https://doi.org/10.1016/j.electacta.2021.138335.

5-4. M. Thuvander, M. Abraham, A. Cerezo, and G. D. W. Smith, Thermal stability of electrodeposited nanocrystalline nickel and iron-nickel alloys, Mater. Sci. Tech. 17 (2013) 961-970. https://doi.org/10.1179/026708301101510799.

5-5. R. A. Andrievski, Review stability of nanostructured materials, J. Mater. Sci. 38 (2003) 1367-1375. https://doi.org/10.1023/A:1022988706296.

5-6. E. Pellicer, A. Varea, K. M. Sivaraman, S. Pane, S. Surinach, M. D. Baro, J. Nogues, B. J. Nelson, and J. Sort, Grain Boundary Segregation and Interdiffusion Effects in Nickel-Copper Alloys: An Effective Means to Improve the Thermal Stability

of Nanocrystalline Nickel, ACS Appl. Mater. Interfaces 3 (2011) 2265-2274. https://doi.org/10.1021/am2004587]

5-7. J. Sudagar, J. Lian, W. Sha,Electroless nickel, alloy, composite and nano coatings - A critical review, J. Alloys Compd. 571 (2013) 183-204. https://doi.org/10.1016/j.jallcom.2013.03.107.

5-8. K. Krishnaveni, T. S. N. Sankara Narayanan, S. K. Seshadri, Corrosion resistance of electrodeposited Ni–B and Ni–B–Si_3N_4 composite coatings, J. Alloys Compd. 480 (2009) 765-770. https://doi.org/10.1016/j.jallcom.2009.02.053.

5-9. K. Krishnaveni, T. S. N. Sankara Narayanan, S. K. Seshadri, Electrodeposited Ni–B coatings: Formation and evaluation of hardness and wear resistance, Mater. Chem. Phys., 99 (2006) 300-308. https://doi.org/10.1016/j.matchemphys.2005.10.028.

5-10. Yu. N. Bekish, S. K. Poznyak, L. S. Tsybulskaya, T. V. Gaevskaya, Electrodeposited Ni-B alloy coatings: Structure, corrosion resistance and mechanical properties, Electrochim. Acta, 55 (2010) 2223-2231. https://doi.org/10.1016/j.electacta.2009.11.069.

5-11. K. Kim, H.-B. Kwon, H.-R. Ahn, Y.-J. Kim, MEMS-based Ni-B probe with enhanced mechanical properties for fine pitch testing, Micro Nano Syst. Lett. 5 (2017) 3. https://doi.org/10.1186/s40486-016-0039-1.

5-12. H.-B. Kwon, K. Kim, H.-R. Ahn, Y.-J. Kim, Electrodeposition and Characterization of Nanocrystalline Ni-B with Low Boron Content for MEMS Applications, Sens. Mater. 29 (2017) 225-234. http://dx.doi.org/10.18494/SAM.2017.1441.

5-13. Watanabe, T. F. M. Chang, M. Schneider, U. Schmid, C. Y. Chen, S. Iida, D. Yamane, H. Ito, K. Machida, K. Masu, M. Sone, Effective Young's Modulus of Complex Three Dimensional Multilayered Ti/Au Micro-Cantilevers Fabricated by Electrodeposition and the Temperature Dependency, Electrochem 2 (2021) 216-223. https://doi.org/10.3390/electrochem2020015.

5-14. K. Krishnaveni, T. S. N. Sankara Narayanan, S. K. Seshadri, Electroless Ni–B coatings: preparation and evaluation of hardness and wear resistance, Surf. Coat. Technol. 190 (2005) 115-121. https://doi.org/10.1016/j.surfcoat.2004.01.038.10.

5-15. H. Ogihara, K. Udagawa, T. Saji, Effect of boron content and crystalline structure on hardness in electrodeposited Ni–B alloy films, Surf. Coat. Technol. 206 (2012) 2933-2940. https://doi.org/10.1016/j.surfcoat.2011.12.025.

5-16. K. H. Lee, D. Chang, S. C. Kwon, Properties of electrodeposited nanocrystalline Ni–B alloy films, Electrochim. Acta 50 (2005) 4538-4543. https://doi.org/10.1016/j.electacta.2004.03.067.

5-17. A. Benyagoub, L. Thomé, A. Audouard, A. Chamberod, K. Królas, P. Wodniecki, Electrical properties of amorphous NI-B films prepared by ion implantation and sputtering, J. Non. Cryst. Solids 87 (1986) 116-122. https://doi.org/10.1016/S0022-3093(86)80073-4.

5-18. R. Oriňáková, K. Rošáková, A. Oriňák, M. Kupková, J. N. Audinot, H.-N. Migeon, J. T. Andersson, K. Kovaľ, Electrodeposition of composite Ni–B coatings in a stirred heterogeneous system. J. Solid. State. Electrochem. 15 (2011) 1159–1168. https://doi.org/10.1007/s10008-010-1177-7.

5-19. V. Vitry, A. -F. Kanta, F. Delaunois, Mechanical and wear characterization of electroless nickel-boron coatings, Surf. Coat. Technol. 206 (2011) 1879-1885. https://doi.org/10.1016/j.surfcoat.2011.08.008.

5-20. U. S. Waware, A. M. S. Hamouda, N. P. Wasekar, Mechanical properties, thermal stability and corrosion behavior of electrodeposited Ni-B/AlN nanocomposite coating, Surf. Coat. Technol. 337 (2018) 335-341. https://doi.org/10.1016/j.surfcoat.2018.01.028.

5-21. S. Ghosh, Electroless copper deposition: A critical review, Thin Solid Films, 669, (2019) 641-658. https://doi.org/10.1016/j.tsf.2018.11.016

5-22. S. Arai, T. Saito, M. Endo, Low-Internal-Stress Nickel Multiwalled Carbon Nanotube Composite Electrodeposited from a Sulfamate Bath, J. Electrochem. Soc. 154 (2007) D530-D533. https://doi.org/10.1149/1.2768285.

5-23. S. Arai, K. Miyagawa, Fabrication of Co-W Alloy/Multiwalled Carbon Nanotube Composite Films by Electrodeposition for Improved Frictional Properties, ECS J. Solid State Sci. Technol. 2 (2013) M39-M43. https://doi.org/10.1149/2.036311jss.

5-24. V. Vitry, J. Hastir, A. Mégret, S. Yazdani, M. Yunacti, L. Bonin, Recent advances in electroless nickel-boron coatings, Surf. Coat. Technol. 429, (2022) 127937

https://doi.org/10.1016/j.surfcoat.2021.127937.

5-25. D. Kiener, W. Grosinger, G. Dehm, R. Pippan, A further step towards an understanding of size-dependent crystal plasticity: In situ tension experiments of miniaturized single-crystal copper samples, Acta Mater. 56, 2008, 580-592. https://doi.org/10.1016/j.actamat.2007.10.015.

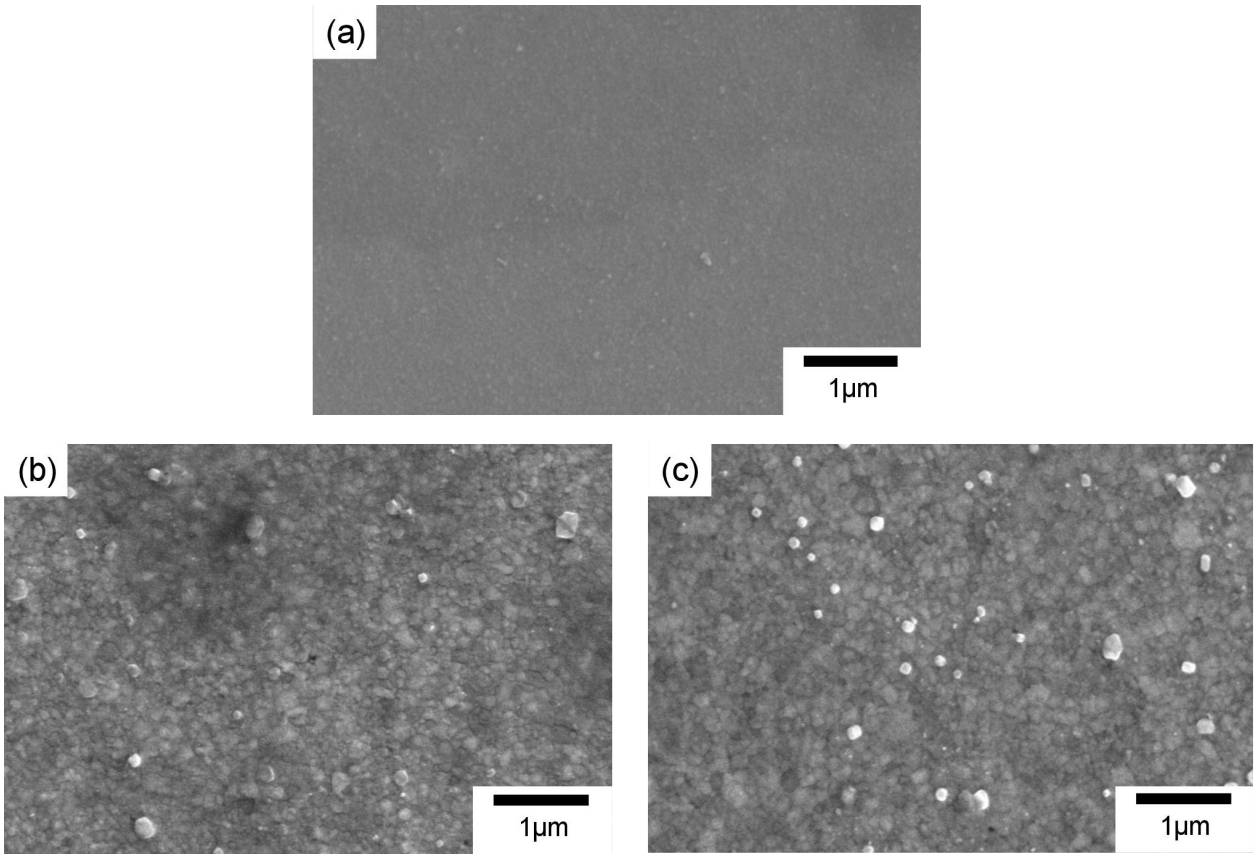

Fig. 5-1 SEM micrographs of (a) as-deposited and heat treated (b) at 250 °C for 2 h and (c) at 250 °C for 4 h Ni-B alloy films electrodeposited at current density of 1 A/dm^2.

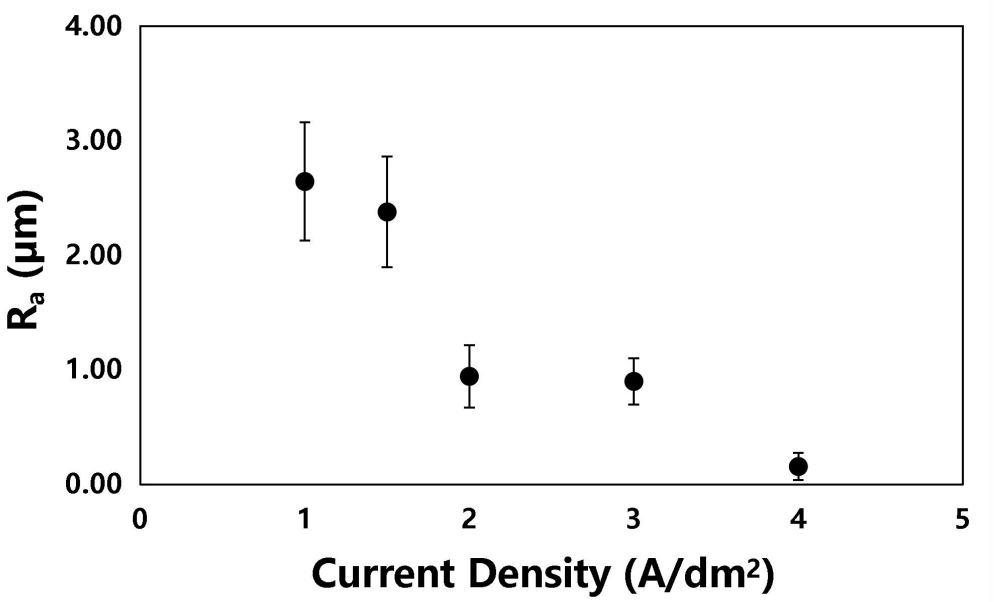

Fig. 5-2 Relationship between the surface roughness (R_a) and the current density.

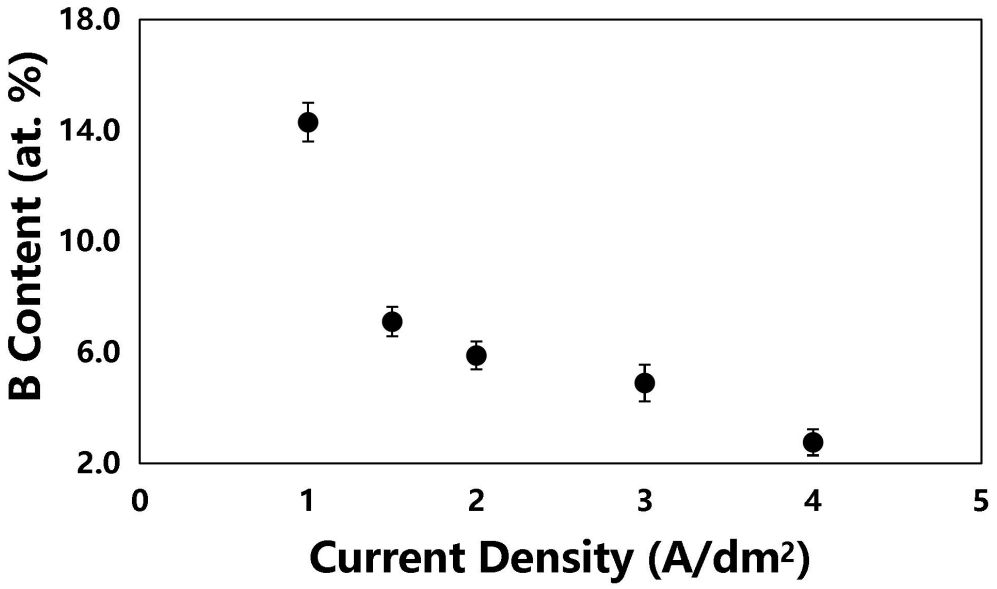

Fig. 5-3 Relationship between the B content and the current density.

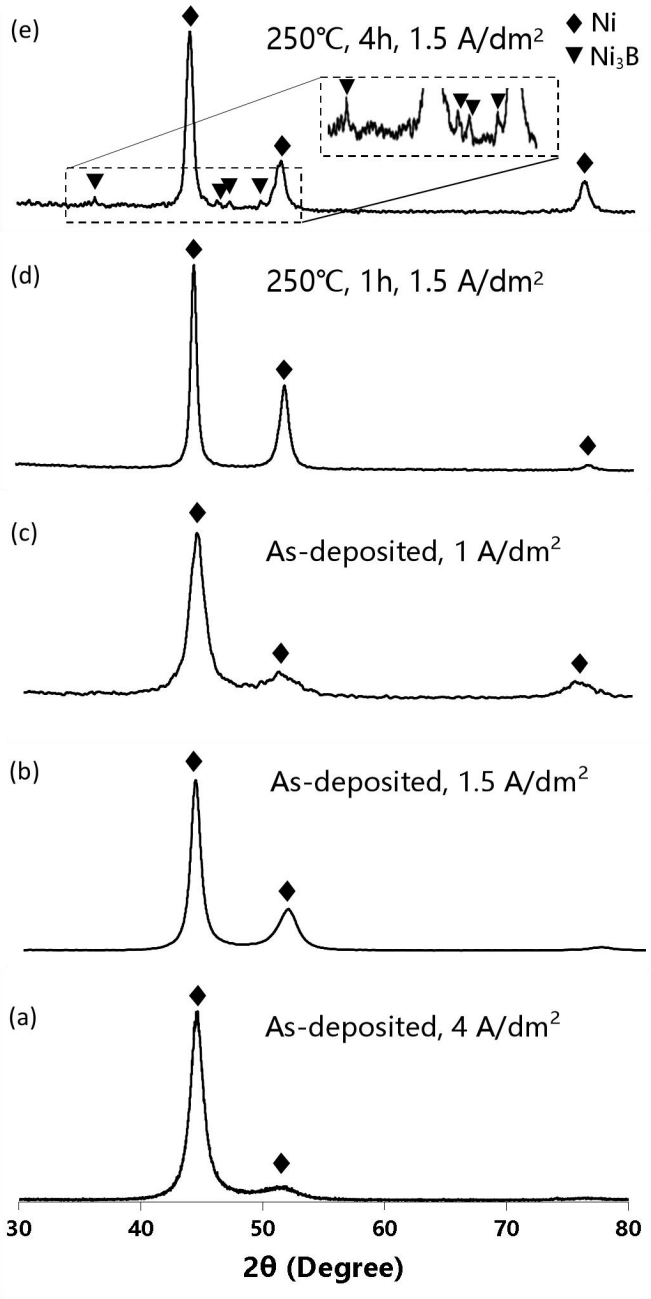

Fig. 5-4 XRD patterns of as-deposited Ni-B alloys (a) deposited at the current density of 4 A/dm^2, (b) 1.5 A/dm^2, (c) 1 A/dm^2; and 250 °C heat-treated Ni-B alloys treated for (d) 1 h and (e) 4 h, deposited at 1.5 A/dm^2.

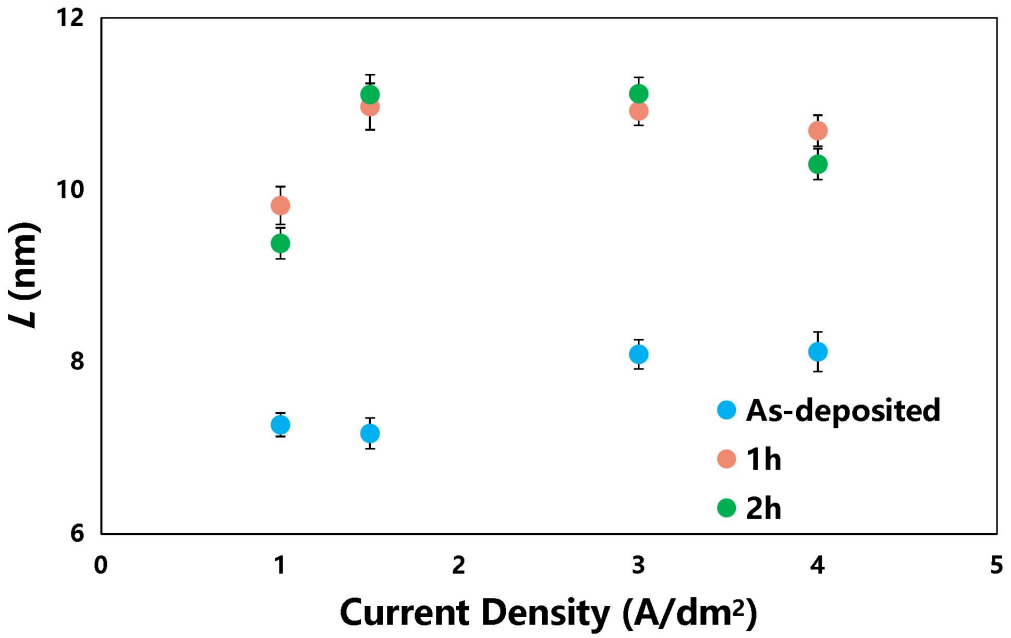

Fig. 5-5 Dependence of L on the current density in as-deposited and heat treated (250 °C) Ni-B alloy films.

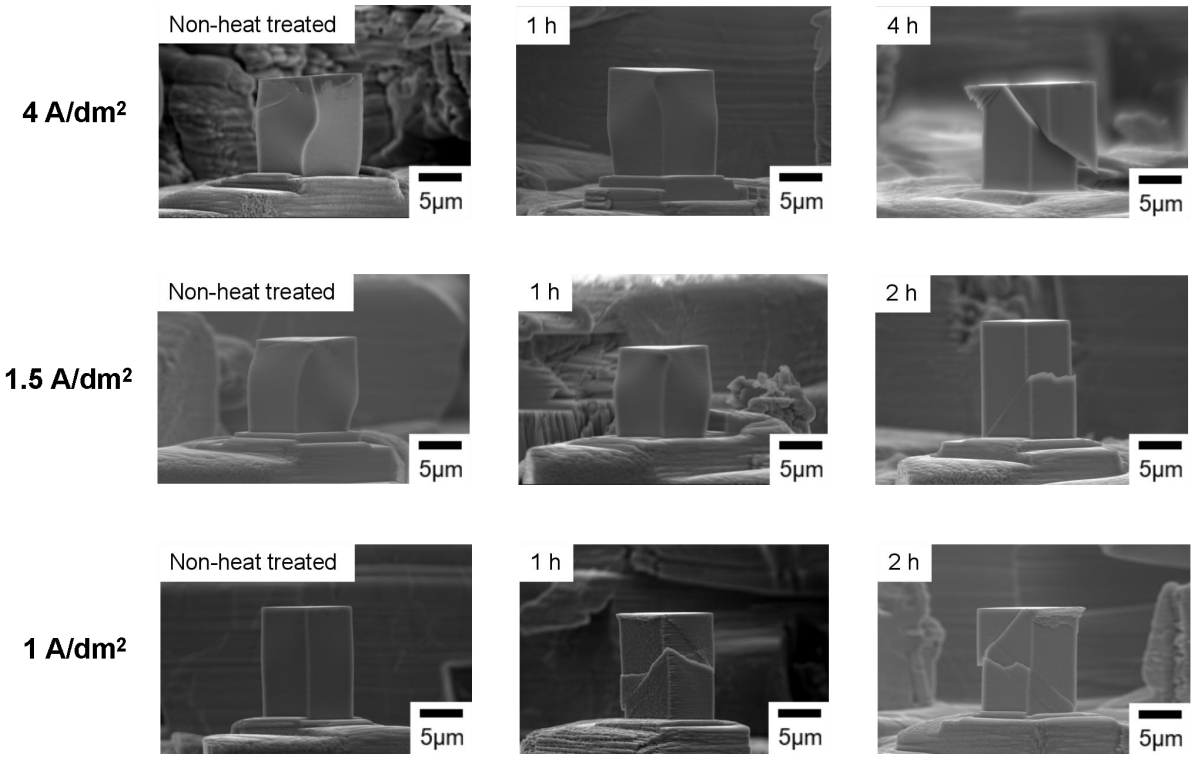

Fig. 5-6 SEM images of the deformed micro-pillars fabricated from as-deposited and heat-treated (250 °C) Ni-B alloy films deposited at different current densities.

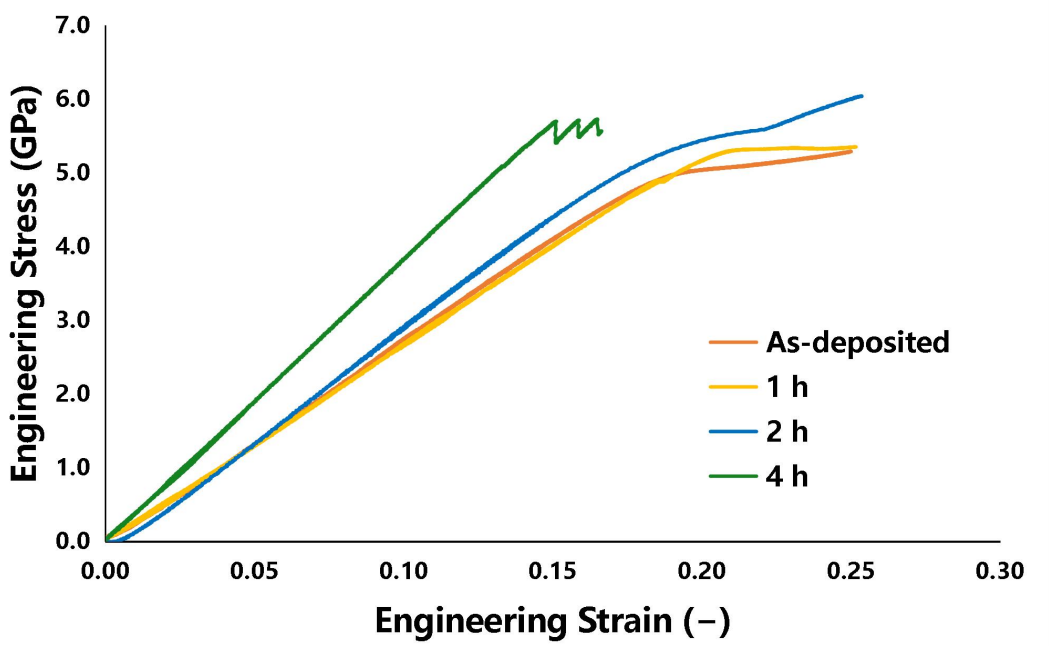

Fig. 5-7 Engineering strain-engineering stress curves generated from micro-compression of the micro-pillars fabricated from the as-deposited and heat-treated (250 °C) Ni-B alloy films deposited at 4 A/dm^2.

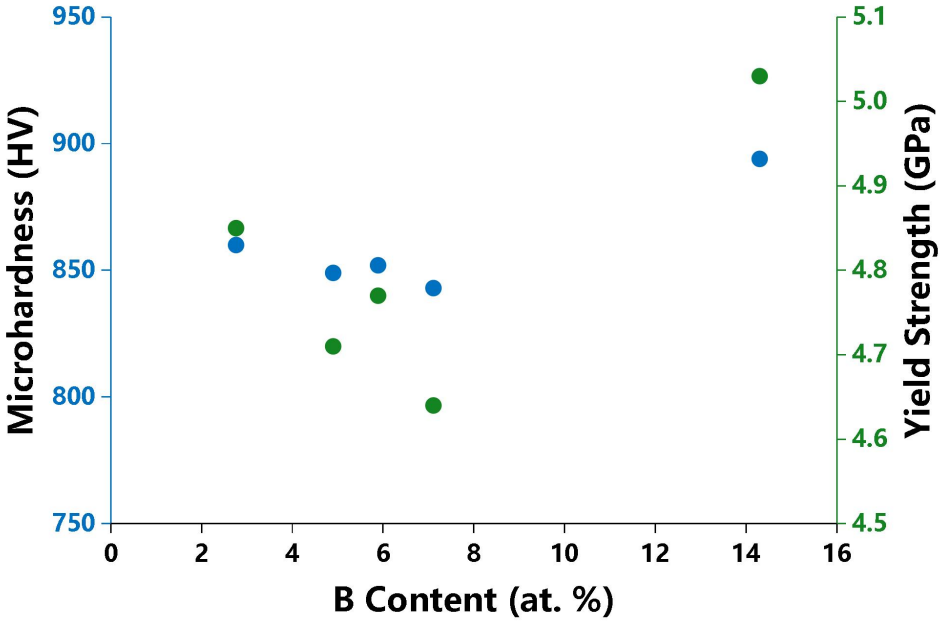

Fig. 5-8 Relationships between the composition, micro-hardness (blue dots) and yield strength (green dots) of as-deposited Ni-B alloy films.

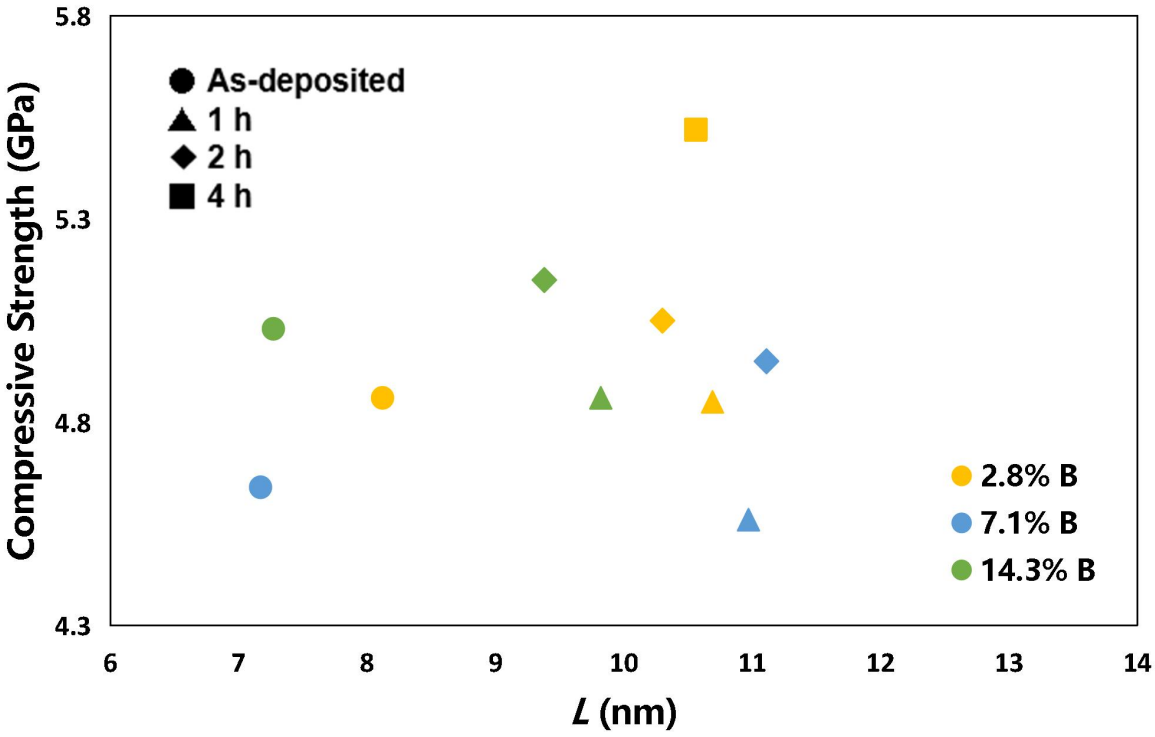

Fig. 5-9 Relationships between the compressive strength and *L* of as-deposited and heat treated (250 °C) Ni-B alloy films.

CHAPTER 6

Specimen Size Effect of Ni-B Alloys

6-1. Introduction

The strengths of metallic materials are known to be dependent on the specimen sizes on micro-scale or nano-scale, which is known as the specimen size effect [6-1~6-3]. For example, in single crystal face centered cubic metals, the strengthening is observed when the extrinsic sample dimensions are reduced below the required distance for dislocation self-duplication. In this case, the conventional dislocation propagation mechanism ceases and the materials are left in a "dislocation-starved state", making the deformation process harder and leading to a size-dependent strength response (Greer et al., 2005) [6-3]. The effect can be described by a power law dependence, $\sigma \propto D^{-n}$, where σ is the strength, D is the specimen size and n is a scaling exponent [6-4~6-6]. In design of structure components in electronic devices, the mechanical property characterization is critical to understand the reliability and structure stability of the structure component. Thus, the specimen size effect has to be considered in the design of micro-scale components in miniaturized devices, such as micro-electro-mechanical system (MEMS) devices.

On the other hand, the experimental results of specimens composed of nanocrystalline metals are divergent. Both smaller-is-weaker and smaller-is-stronger

specimen size effects are reported. For instance, following a decrease in the specimen size, the strength of nanocrystalline nickel-tungsten nano-pillars was reported to decrease from 1.47 GPa to 0.86 GPa [6-7], while a strengthening specimen size effect was reported in 60 nm grained nanocrystalline nickel [6-8]. The specimen size effect in nanocrystalline materials is reported to be depended on the critical size ratio, D/d, where D is the specimen size and d is the grain size. Gu et al. proposed a model which assumes that only the grains distributed on the outer sample surface contribute to the specimen size effect [6-9]. When D/d is large, the strength approaches the strength of a bulk-size specimen. For $D/d \approx 1$, a weakening effect is observed due to the grain boundary sliding mechanism. Zhu et al. proposed an assumption that the specimen size effect can switch from strengthening to weakening by reducing D/d below a critical value through molecular dynamics simulation [6-10]. The difference in the specimen size effects is considered to be a result of the competition between different mechanisms, including the surface strengthening, grain boundary mediated deformation and dislocation mediated deformation.

Emerging focused ion beam milling and micro-mechanical testing technology provide ways for precise evaluation of the mechanical property on micro- and nano-scale [6-11, 6-12]. A previous study has reported the micro-mechanical properties of nickel-phosphorus alloy films, and a smaller-is-stronger specimen size effect was observed in 300 °C heat-treated nickel-phosphorus alloys. The fracture strength increased from 3.1 GPa to 4.7 GPa when cross-section of the micro-specimen reduces from $20 \times 20\ \mu m^2$ to $10 \times 10\ \mu m^2$ [6-12].

Nickel-boron alloys are reported to show excellent mechanical strength, wear resistance and thermal characteristic and have a great application potential in the miniaturized electronics [6-13, 6-14]. Nickel-boron alloy films can be easily fabricated through electrodeposition method, and the alloy film deposition can be easily integrated with existing micro-scale components fabrication techniques [6-15, 6-19]. Besides, the formation of intermetallic compounds Ni_3B have in heat-treated nickel-boron alloys could further enhance the mechanical strength by the precipitation strengthening mechanism as reported in a previous study [6-17]. However, the specimen size effect on the strength and deformation mode of as-deposited and heat-treated nickel-boron alloy still remain unknown. Also, cylinder shaped pillars with tapering angles are commonly used in studies on the specimen size effect. The tapering angle may result an over/underestimation of the strength [6-18].

Therefore, the specimen size effect on mechanical properties of electrodeposited nickel-boron alloys is evaluated by micro-compression test using non-tapered pillar type micro-specimens in this work. The mechanical strength is determined from the engineering stress-engineering strain curve generated from the micro-compression test. The nickel-boron alloys are annealed at different temperatures to evaluated influences of the Ni_3B. Micro-specimens with different sizes are fabricated from the as-electrodeposited and annealed nickel-boron alloys by focus ion beam system. The changes in the deformation mode of different alloys are also observed and discussed.

6-2. Experimental

The nickel-boron alloys were prepared by electrodeposition method. The alloy films were annealed at 250 °C and 400 °C in a vacuum atmosphere of < 0.1 Pa for 4 h using a vacuum furnace (FT-01VAC-30, FULL-TECH Co., Ltd., Osaka, Japan). Crystalline characteristics of the nickel-boron alloys were evaluated by an X-ray diffractometer (XRD, Ultima IV, Rigaku Corp., Tokyo, Japan).

The pillar type micro-specimens were fabricated from the nickel-boron alloy films by a focus ion beam system (FIB, FB2100, Hitachi, Japan). The micro-specimen had a non-tapered cuboid shape with dimensions of 4 μm × 4 μm × 8 μm, 8 μm × 8 μm × 16 μm, 12 μm × 12 μm × 24 μm and 16 μm × 16 μm × 32 μm. The aspect ratio (height/length of the square cross-section) of the micro-specimen was maintained at 2. The length of the square cross-section is denoted as the specimen size h. At least 2 micro-specimens of each designed size were fabricated from each alloy. Exact sizes of the micro-specimens were measured by a scanning electron microscope (SEM, SU4300SE Hitachi Co., Ltd., Japan). Observations of the micro-specimens of each designed size were fabricated from each alloy. Exact sizes of the micro-specimens were conducted through the SEM. The uniaxial compression test was conducted using a specially designed test system, which was equipped with a flat-topped indenter. To eliminate the effects of strain gradients, the strain rate was kept at 6.25×10^{-3} μm/s in all the tests.

6-3. Crystalline structure

XRD measurement was conducted to characterize the crystalline structure of as-deposited and annealed nickel-boron alloys. The XRD patterns of different alloys are shown in Fig. 1. Peak sharpening was confirmed after both 250 °C and 400 °C annealing, which indicated an improvement in the crystallinity of the nickel-rich matrix. Besides, several diffraction peaks appeared in the range of $2\theta = 35° \sim 50°$ after the 400 °C annealing. These new peaks are suggested to be contributed by the precipitation of intermetallic compound Ni_3B. The grain size of annealed alloys calculated by Scherrer equation is 10.8 nm and 23.3 nm for 250 °C and 400 °C, respectively.

6-4. Deformation mode

SEM images of the nickel-boron micro-specimens with different dimensions after the compression test are shown in Fig. 2. All micro-specimens fabricated from the as-deposited nickel-boron alloys exhibited a typical ductile deformation mode. The deformation mode switched to a brittle fracture behavior after the annealing at 250 °C. On the other hand, the micro-specimens showed a ductile fracture failure mode with improved plasticity after the annealing at 400 °C. The sign of shear bands can still be observed from Fig. 2(e) and 2(f).

6-5. Strength

Engineering stress-engineering strain curves generated from compression tests of different micro-specimens are shown in Fig. 3. For micro-specimens which showed a ductile deformation (as-deposited and 400 °C annealed), the 0.2% offset yield strengths were regarded as their compressive strengths [6-19]. For the brittle ones, their

compressive strengths were defined as the fracture strength when the first shear band occurred. A maximum compressive strength of 5.79 GPa was confirmed in the alloy after 4 h of annealing at 250 °C, with a high elastic limit of ca. 14%. On the contrary, the ductile deformed ones only showed a elastic limit below 10%. Engineering stress-engineering strain curves of the micro-specimens prepared from the 400 °C annealed nickel-boron alloy are shown in Fig. 4. A strain softening after the yield point was observed in all specimens due to the formation of shear bands and the ductile fracture. We can find that the failure strength increased as *h* decreasing, while the elastic limit increased as *h* increasing.

The as-deposited nickel-boron alloy showed a typical ductile compressive deformation mode. In the case of the 250 °C annealed alloy, precipitation of intermetallic compound Ni_3B caused a significant increase in the flow stress due to precipitation strengthening. During the compression, the increasing loading firstly reached the stress required to drive shear band propagation, and led to a catastrophic failure. Regarding the 400 °C annealed alloy, an increase in the grain size was confirmed through the XRD evaluation. In this case, values of the flow stress became smaller and closer to those needed to induce fracture processes. When the plastic flow is intensive, nanocracks formed in a specimen gradually transform into nanovoids and microvoids and locate in one section of the specimen [6-20]. Then, ductile fracture occurs through coalescence of the microvoids shortly after the yield point.

Relationships between the compressive strength and the specimen size *h* are shown in Fig. 5. A strengthening effect was observed after the annealing at 250 °C basically due to the precipitation strengthening effect by Ni_3B, while a softening effect was found

after the annealing at 400 °C. The weakening effect in the 400 °C annealed alloy is considered to be a result of coarsened nickel-rich matrix, the enlarged grain size caused a decrease in the flow stress following the Hall-Petch relationship. Meanwhile, the aggregation of Ni_3B particles may also reduce the reinforcement sites in the entire alloy specimen. All types of micro-specimens showed a smaller-is-stronger specimen size effect. Among the three alloys, 250 °C annealed one gave a largest scaling exponent of 0.149, and as-deposited alloy gave a smallest scaling exponent of 0.109.

For brittle materials, the stress to trigger shear band propagation is expected to be related to the probability of having weak flaws in the specimen, which depends on the specimen volume. The existence of weak flaws such as nanocracks, inclusions and surface irregularities would act as stress concentration sites. Then flaws located in one specimen section converge and result in brittle intergranular fracture [6-20]. In this case, Weibull statistics could be used to describe the dependence of the failure stress on the specimen size.

According to Weibull statistics [6-21], the probability of failure in a material under a given uniaxial stress, σ , is:

$$P_f = 1 - \exp\left[-V \left(\frac{\sigma}{\sigma_0} \right)^m \right] \tag{1}$$

where σ_0 is a scaling parameter, m is the Weibull modulus, and V is the volume of the specimen. Assume the fracture probability caused by the weak flaw in samples with different dimensions are the same, i.e., P_f = constant, the equation is arranged to the following:

$$V\left(\frac{\sigma}{\sigma_0}\right)^m = const. \tag{2}$$

$$m\ln\sigma = const. - \ln V \tag{3}$$

Hence, the Weibull statistics can be plotted as $-\ln V$ vs. $\ln\sigma$, as shown in Fig. 6. The fitting gave a Weibull modulus m = 18.014. Weibull statistics has also been used to describe the strength of brittle materials in other studies. For example, Jang et al. repored m = 10.84 in $Zr_{35}Ti_{30}Co_6Be_{29}$ metallic glasses and Wu et al. reported m = 25.5 in $(Zr_{48}Cu_{45}Al_7)_{98}Y_2$ metallic glasses [6-22]. Generally, lower Weibull modulus implies higher flaw-sensitivity, and hence a stronger dependence on the specimen size. Therefore, the specimen size effect of brittle samples reported in this study could be attributed to the lower probability of having weak flaws in smaller samples.

Regarding ductile fractured ones, the size dependence of their yield strengths can also be explained by the existence of weak flaws in samples having a different volume. The deformation is considered to be caused by collaboration of plastic flow and shear band propagation. In the case of the 400 °C annealed alloy, the ductile fracture type failure is greatly affected by the weak flaws, and hence exhibited an obvious specimen size effect (scaling exponent of 0.143), which is close to the one in the 250 °C annealed alloy. On the contrary, as-deposited nickel-boron alloys showed a ductile deformation mode with the least contribution by flaw-induced shear band propagation. The specimen size effect in this case is considered to be a result of grain boundary sliding dominated mechanism. Deformation initiation sites in nanocrystals are depleted when the specimen

size becomes small, which results an increase in the yield strength [6-8]. Nagoshi et al. also reported a smaller-is-stronger specimen size effect in 60 nm grained nanocrystalline nickel and gave a similar scaling exponent of 0.125 [6-8]. Unlike single crystals commonly show a scaling exponent between 0.5 and 0.7 [6-4~6-6], the specimen size effect in nanocrystalline materials is suggested to be much weaker due to different deformation mechanisms.

6-6. Chapter Summary

Electrodeposited nickel-boron alloys with boron content of 0.52 wt.% were fabricated into pillar type micro-specimens for micro-compression test to investigate the specimen size effect on their mechanical strength. As-deposited nickel-boron alloy exhibited a ductile compressive deformation mode. The deformation mode switched to a brittle fracture type catastrophic failure after the annealing at 250 °C with improved elastic limit. On the other hand, the micro-specimens fabricated from 400 °C annealed alloy showed a ductile fracture deformation mode and improved plasticity comparing to 250 °C annealed ones.

As-deposited nickel-boron alloy exhibited a high yield strength and ductile compressive deformation mode. An increase in the failure strength was confirmed after the annealing at 250 °C due to the precipitation strengthening of the intermetallic compound Ni_3B. On the other hand, a softening effect was observed after the annealing at 400 °C. A small-is-stronger specimen size effect was confirmed as the specimen size decreased. The fracture strength of 250 °C annealed alloys increased from 4.64 GPa to

5.63 GPa as the extrinsic specimen size h reduced from 16 μm to 4 μm. Through the Weibull statistics, we find that the micro-specimens showed flaw-sensitivity, and the dependence of their strength on the specimen size can be explained by the lower probability of having weak flaws in smaller specimens.

References

6-1. M. D. Uchic, D. M. Dimiduk, J. N. Florando, W. D. Nix, Sample Dimensions Influence Strength and Crystal Plasticity, Science 305 (2004) 986-989. https://doi.org/10.1126/science.1098993.

6-2. D. Kiener, W. Grosinger, G. Dehm, R. Pippan, A further step towards an understanding of size-dependent crystal plasticity: In situ tension experiments of miniaturized single-crystal copper samples, Acta Mater. 56, 2008, 580-592. https://doi.org/10.1016/j.actamat.2007.10.015.

6-3. J. R. Greer, W. C. Oliver, W. D. Nix, Size dependence of mechanical properties of gold at the micron scale in the absence of strain gradients, Acta Mater. 53 (2005) 1821-1830. https://doi.org/10.1016/j.actamat.2004.12.031.

6-4. A. T. Jennings, M. J. Burek, J. R. Greer, Microstructure Versus Size: Mechanical Properties of Electroplated Single Crystalline Cu Nanopillars, Phys. Rev. Lett., 104 (2010) 135503. https://doi.org/10.1103/PhysRevLett.104.135503.

6-5. R. Dou, B. Derby, A Universal Scaling Law for the Strength of Metal Micropillars and Nanowires, Scr. Mater., 61 (2009) 524-527. https://doi.org/10.1016/j.scriptamat.2009.05.012.

6-6. J. R. Greer, D. Jang, X. W. Gu, Exploring Deformation Mechanisms in Nanostructured Materials, JOM 64 (2012) 1241-1252. https://doi.org/10.1007/s11837-012-0438-6.

6-7. D. Jang, J. R. Greer, Size-induced weakening and grain boundary-assisted deformation in 60 nm grained Ni nanopillars, Scr. Mater. 64 (2011) 77-80. https://doi.org/10.1016/j.scriptamat.2010.09.010.

6-8. T. Nagoshi, M. Mutoh, T. F. M. Chang, S. Tatsuo, M. Sone, Sample size effect of electrodeposited nickel with sub-10 nm grain size, Mater. Lett. 117 (2014) 256-259. https://doi.org/10.1016/j.matlet.2013.12.017.

6-9. X. W. Gu, C. N. Loynachan, Z. Wu, Y.-W. Zhang, D. J. Srolovitz, J. R. Greer, Size-Dependent Deformation of Nanocrystalline Pt Nanopillars, Nano Lett., 12 (2012) 6385-6392. https://doi.org/10.1021/nl3036993.

6-10. Y. Zhu, Z. Li, M. Huang, Coupled effect of sample size and grain size in polycrystalline Al nanowires, Scripta Mater. 68 (2013) 663-666. https://doi.org/10.1016/j.scriptamat.2013.01.029.

6-11. T. Nagoshi, T. F. M. Chang, S. Tatsuo, M. Sone, Mechanical properties of nickel fabricated by electroplating with supercritical CO_2 emulsion evaluated by micro-compression test using non-tapered micro-sized pillar, Microelectron. Eng. 110 (2013) 270-273. https://doi.org/10.1016/j.mee.2013.02.001.

6-12. T. Hotta, T. F. M. Chang, C. Y. Chen, H. Sawae, Y. Imada, M. Mizoguchi, O. Kudo, R. Maeda, M. Sone, Micro-Compression Characterization and Thermal Stability of Electrolessly Plated Nickel Phosphorus Alloy, ECS J. Solid State Sci. Technol. 10 (2021) 035007. https://doi.org/10.1149/2162-8777/abedd3.

6-13. Yu. N. Bekish, S. K. Poznyak, L. S. Tsybulskaya, T. V. Gaevskaya, Electrodeposited Ni-B alloy coatings: Structure, corrosion resistance and mechanical

properties, Electrochim. Acta, 55 (2010) 2223-2231. https://doi.org/10.1016/j.electacta.2009.11.069.

6-14. K. H. Lee, D. Chang, S. C. Kwon, Properties of electrodeposited nanocrystalline Ni-B alloy films, Electrochim. Acta 50 (2005) 4538-4543. https://doi.org/10.1016/j.electacta.2004.03.067.

6-15. H.-B. Kwon, K. Kim, H.-R. Ahn, Y.-J. Kim, Electrodeposition and characterization of nanocrystalline Ni-B with low boron content for MEMS applications, Sens. Mater. 29 (2017) 225-234. http://dx.doi.org/10.18494/SAM.2017.1441.

6-16. Y. Jiang, C. Y. Chen, T. Kurioka1, X. Luo, D. Yamane, M. Mizoguchi, O. Kudo, R. Maeda, M. Sone, T. F. M. Chang, Electrodeposition of Ni-B Alloy Film: Effect of Current Density and Heat Treatment on Micro-Mechanical Property, J. Electrochem. Soc. 169 (2022) 112504. https://doi.org/10.1149/1945-7111/ac9dc2.

6-17. B. E. Schuster, Q. Wei, T. C. Hufnagel, K. T. Ramesh, Size-independent strength and deformation mode in compression of a Pd-based metallic glass, Acta Mater. 56 (2008) 5091-5100. https://doi.org/10.1016/j.actamat.2008.06.028.

6-18. H. Zhang, B. E. Schuster, Q. Wei, K. T. Ramesh, The design of accurate micro-compression experiments, Scr. Mater. 54 (2006) 181-186. https://doi.org/10.1016/j.scriptamat.2005.06.043.

6-19. W. F. Hosford, Mechanical Behavior of Materials, 2nd edition, Cambridge University Press, New York, 2010.

6-20. I. A. Ovid'ko, Review on the fracture processes in nanocrystalline materials, J. Mater. Sci. 42 (2007) 1694-1708. https://doi.org/10.1007/s10853-006-0968-9.

6-21. C. J. Lee, J. C. Huang, Sample size effect and microcompression of $Mg_{65}Cu_{25}Gd_{10}$ metallic glass, Appl. Phys. Lett. 91 (2007) 161913. https://doi.org/10.1063/1.2800313

6-22. D. Jang, C. T. Gross, J. R. Greer, Effects of size on the strength and deformation mechanism in Zr-based metallic glasses, Int. J. Plast. 27, (2011) 858-867. https://doi.org/10.1016/j.ijplas.2010.09.010.

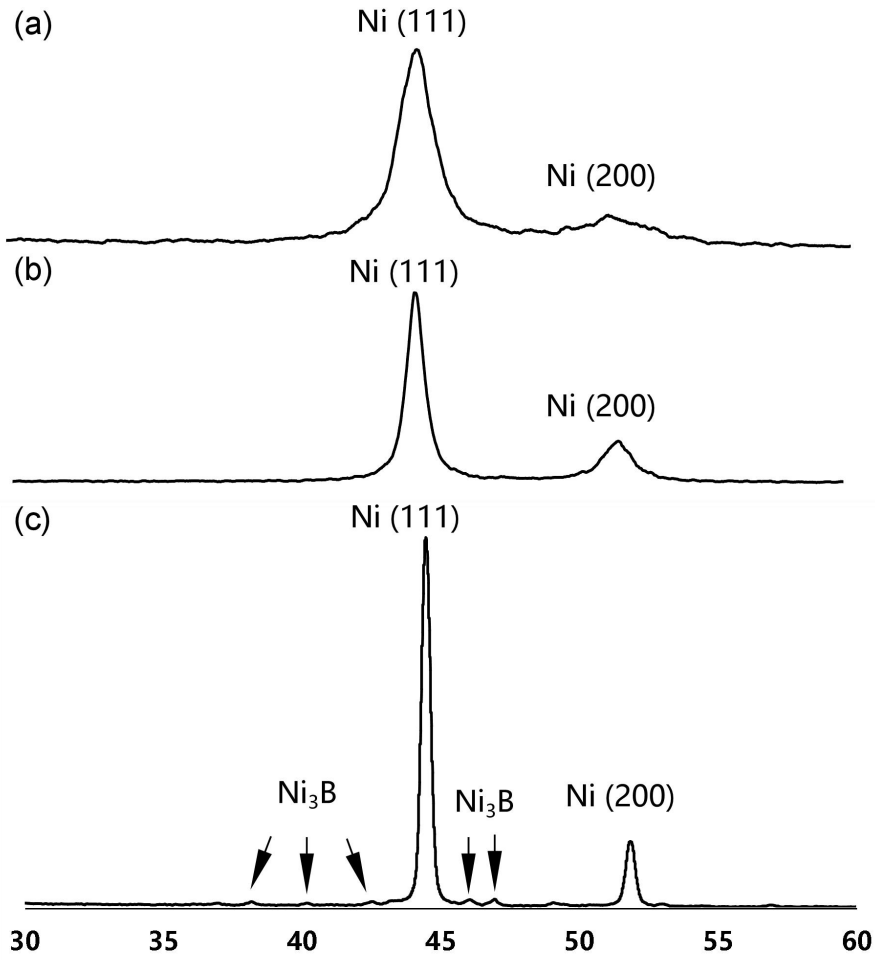

Fig. 6-1 XRD patterns of (a) as-deposited, (b) 250 °C, 4 h and (c) 400 °C, 4 h annealed nickel-boron alloys.

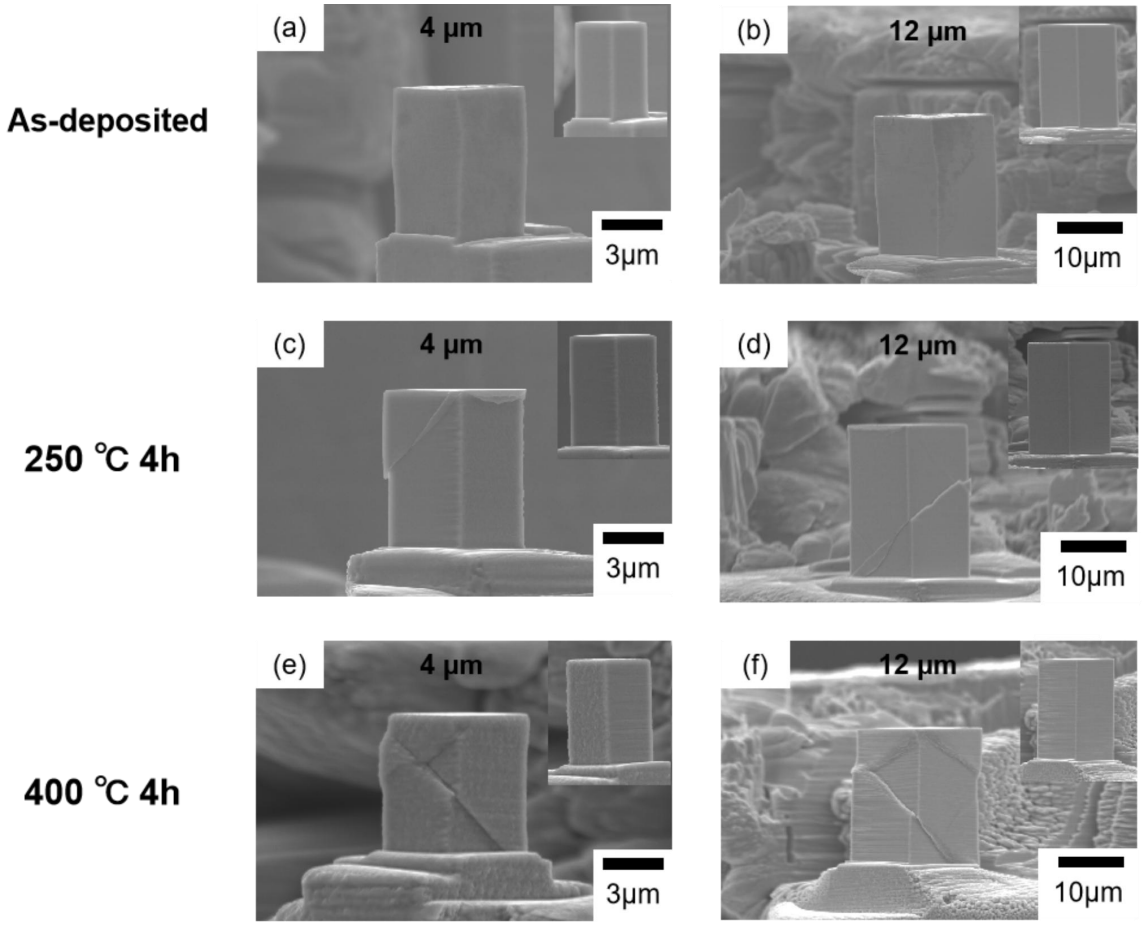

Fig. 6-2 SEM micrographs of the deformed micro-specimens fabricated from as-deposited and annealed nickel-boron alloys with two different dimensions of h = 4 μm and h = 12 μm. (a) as-deposited, h = 4 μm, (b) as-deposited, h = 12 μm, (c) 250 °C, h = 4 μm, (d) 250 °C, h = 12 μm, (e) 400 °C, h = 4 μm, (f) 400 °C, h = 12 μm. Inset images are the corresponding SEM micrographs of the micro-specimens before compression.

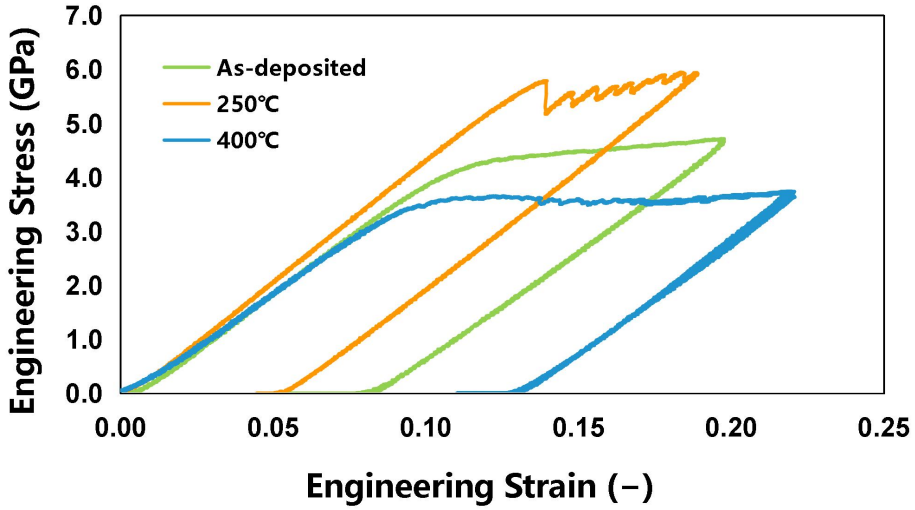

Fig. 6-3 Stress-strain curves of compression tests of micro-specimens fabricated from as-deposited and annealed nickel-boron alloy with the specimen size of h = 4μm.

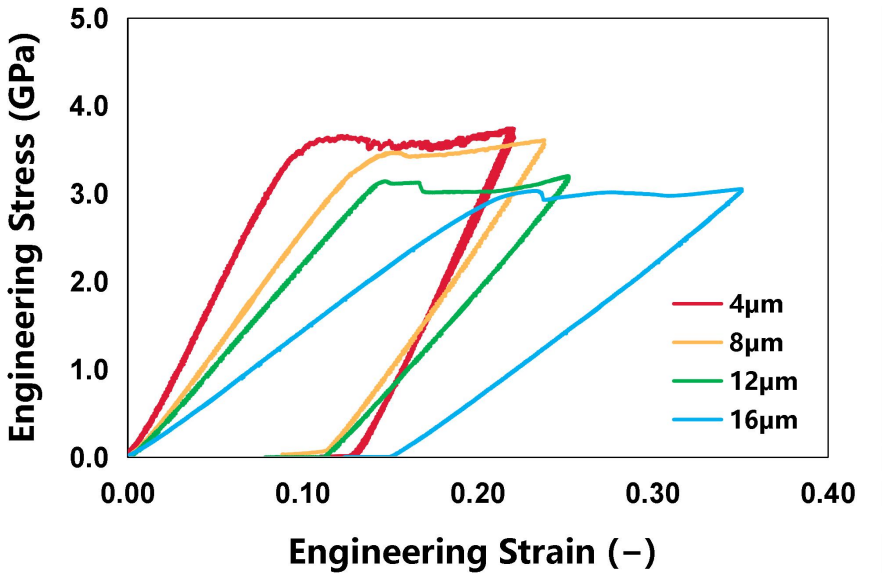

Fig. 6-4 Stress-strain curves of compression tests of micro-specimens fabricated from 400 °C annealed nickel-boron alloy with different specimen sizes of *h*.

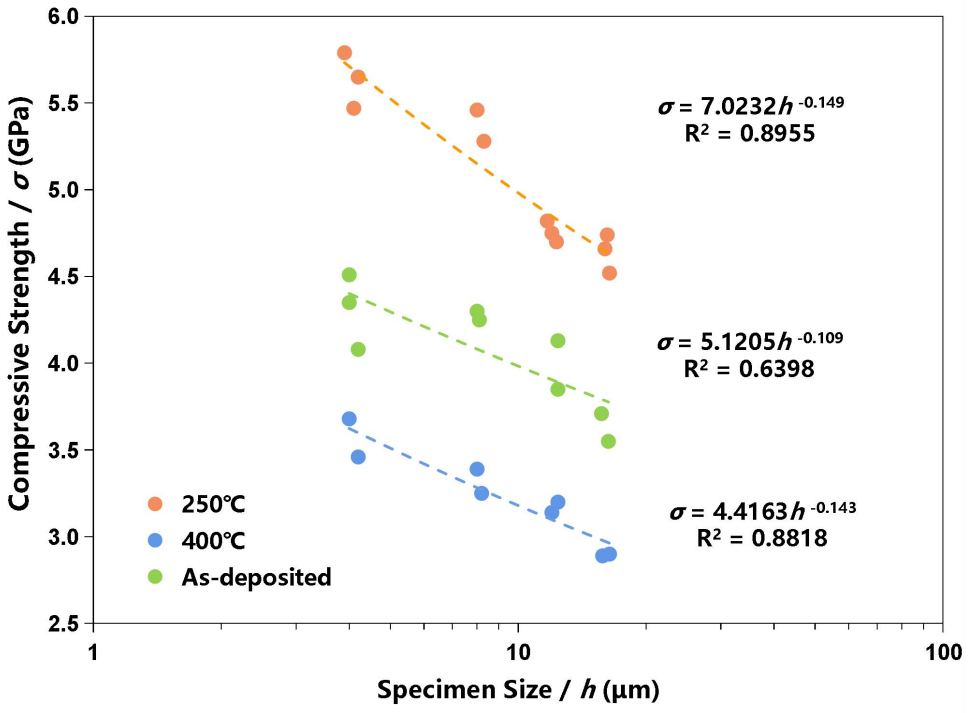

Fig. 6-5 Relationships between the compressive strength and the specimen size *h*.

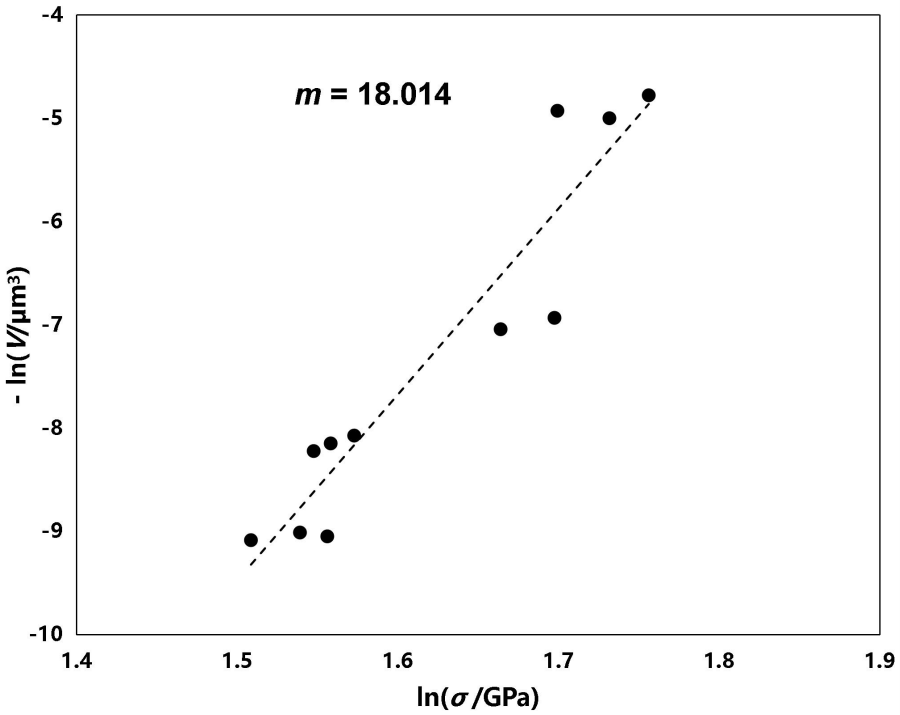

Fig. 6-6 Weibull plots of compressive strengths of nickel-boron alloys.

CHAPTER 7

Conclusions

In this thesis, Ni alloy films were produced by electrodeposition method.

In chapter 2, the Co content was found to increase from ca. 20 to 60 at.% after introduction of $NiBr_2$. Refinement in the average grain size was observed after addition of a surface brightener (NSF-E) into the bath. The micro-hardness was confirmed to be affected by both of the grain size due to the grain boundary strengthening and the alloy composition due to the solid solution strengthening, and the dependency was higher on the grain size. The microhardness reached 548 Hv in a Ni-Co alloy deposit having 13.6 nm grain size and 66.64 at.% Co content.

In chapter 3, micro-mechanical properties of electrodeposited nickel-cobalt alloys were reported in this study to provide design information of micro-components in MEMS. Micro-compression test was conducted using micro-pillar type specimens to investigate the mechanical strength on the micro-scale. The yield strength was found to be highly dependent on the average grain size based on the grain boundary strengthening mechanism. The cobalt content also showed some influences on the yield strength indicating a contribution from the solid-solution strengthening mechanism. The

highest yield strength at 2.37 GPa was obtained from a micro-pillar fabricated from an alloy electrodeposited with the sulfamate bath containing nickel bromide and the Surf-Bright, with an average grain size of 13.6 nm and composed of 58.48 at.% of cobalt.

In chapter 4, effects of bromide ions in the Ni-Co alloy electrodeposition were studied. The presence of bromide ions further promoted the anomalous codeposition behavior in Ni-Co alloy electrodeposition, and led to a significant increase in the Co content, which the Co content increased from 30 at.% to 60 at.% after the addition of NaBr. The bromide ions were found to work as the accelerator in the reduction of cobalt and suppressed the reduction of nickel. By changing pH of the electrolyte, the alloy electrodeposition was confirmed to be affected by the hydroxide ion intermediates generated at cathode. The anomalous codeposition behavior was found to be promoted in a lower pH environment. The introduction of bromide ions and the low pH environment resulted a synergistic effect to the anomalous codeposition behavior.

In chapter 5, Ni-B alloy films with the B content ranged from 2.8 at.% to 14.3 at.% were electrodeposited by controlling the current density. Micro-compression test was conducted to appraise the micro-mechanical strength. As-deposited Ni-B alloy films showed high yield strengths in a range of 4 GPa to 5 GPa and ductile deformation behaviors. The high strength was further enhanced after the 250 °C heat treatment, and a maximum fracture strength of 5.52 GPa was obtained owing to the precipitation strengthening effect by the intermetallic compound, Ni_3B. The electrodeposited Ni-B alloy films showed an excellent micro-mechanical strength and thermal stability and demonstrated the applicability toward miniaturized electronics.

In chapter 6, electrodeposited nickel-boron alloys with boron content of 0.52 wt.% were fabricated into pillar type micro-specimens for micro-compression test to investigate the specimen size effect on their mechanical strength. As-deposited nickel-boron alloy exhibited a high yield strength and ductile compressive deformation mode. A small-is-stronger specimen size effect was confirmed as the specimen size decreased. The fracture strength of 250 °C annealed alloys increased from 4.64 GPa to 5.63 GPa as the extrinsic specimen size h reduced from 16 μm to 4 μm. Through the Weibull statistics, we find that the micro-specimens showed flaw-sensitivity, and the dependence of their strength on the specimen size can be explained by the lower probability of having weak flaws in smaller specimens.

In summary, Ni-Co and Ni-B alloy films were fabricated by eletrcodeposition method. The morphology, crystal structure and composition were controlled by varying the electrodeposition parameters including the current density, pH and additives. The effects of additive NaBr on the Ni-Co electrodeposition were studied by electrochemical analytical methods in this work, the bromide ions were found to work as the accelerator in the reduction of cobalt and suppressed the reduction of nickel. Effects of the pH are also investigated to provide possible explanation to the phenomenon observed, and the anomalous codeposition behavior becomes more obvious in a more acidic electrolyte.

Micro-mechanical properties of electrodeposited Ni-Co and Ni-B alloys were studied by micro-compression test was conducted using micro-pillar type specimens to investigate the mechanical strength on the micro-scale. The yield strength was found to be highly dependent on the average grain size and the alloy composition. A small-is-stronger specimen size effect was confirmed as the specimen size decreased.

List of Achievements

Papers:

1. **Yiming Jiang**, Chun-Yi Chen, Tso-Fu Mark Chang, Xun Luo, Daisuke Yamane, Masato Sone. Electrodeposition of Ni-Co Alloys and the Mechanical Properties by Micro-Vickers Hardness Test, Electrochem, MDPI, Vol. 2, No. 1, pp. 1-9, Jan. 2021.

2. **Yiming Jiang**, Chun-Yi Chen, Xun Luo, Daisuke Yamane, Masanori Mizoguchi, Osamu Kudo, Ryu Maeda, Masato Sone, Tso-Fu Mark Chang. Electrodeposition and Micro-Mechanical Property Characterization of Nickel-Cobalt Alloys toward Design of MEMS Components, Electrochem, MDPI, Vol. 3, pp. 198-210, Apr. 2022.

3. **Yiming Jiang**, Chun-Yi Chen, Tomoyuki Kurioka, Xun Luo, Daisuke Yamane, Masanori Mizoguchi, Osamu Kudo, Ryu Maeda, Masato Sone, Tso-Fu Mark Chang. Electrodeposition of Ni-B Alloy Film: Effect of Current Density and Heat Treatment on Micro-Mechanical Property, Journal of The Electrochemical Society, The Electrochemical Society, Vol. 169, No. 11, pp. 112504, Nov. 2022.

International Conferences:

1. Yiming Jiang, Chun-Yi Chen, Tso-Fu Mark Chang, Xun Luo, Daisuke Yamane, Masanori Mizoguchi, Osamu Kudo, Ryu Maeda, Masato Sone. Micro-Mechanical Characterization of Electrodeposited Ni-Co Alloys toward Design of MEMS Components, Micro and Nano Engineering Conference 2021 (MNE2021), Sept. 2021.
2. Yiming Jiang, Chun-Yi Chen, Xun Luo, Daisuke Yamane, Masanori Mizoguchi, Osamu Kudo, Ryu Maeda, Masato Sone, Tso-Fu Mark Chang. Electrodeposition of Nickel-Cobalt Alloy Films and their Micro-Mechanical Property, TACT2021 International Thin Films Conference, TACT2021 International Thin Films Conference, Nov. 2021.
3. Yiming Jiang, Chun-Yi Chen, Tso-Fu Mark Chang, Xun Luo, Daisuke Yamane, Masanori Mizoguchi, Osamu Kudo, Ryu Maeda, Masato Sone. Electrodeposition of Ni-Co Alloys from Sulfamate Bath and the Micro-Mechanical Property, The 2021 International Chemical Congress of Pacific Basin Societies (Pacifichem 2021), Dec. 2021.
4. Yiming Jiang, Chun-Yi Chen, Xun Luo, Daisuke Yamane, Masanori Mizoguchi, Osamu Kudo, Ryu Maeda, Masato Sone, Tso-Fu Mark Chang. Thermal Stability and Mechanical Property of Electrodeposited Ni-B Alloy, 31st Topical Meeting of the International Society of Electrochemistry, May 2022.
5. Yiming Jiang, Chun-Yi Chen, Tomoyuki Kurioka, Daisuke Yamane, Masanori Mizoguchi, Osamu Kudo, Ryu Maeda, Masato Sone, Tso-Fu Mark Chang. Micro-scale Mechanical Characterustic of Electrodeposited Ni-B Alloys

Components Toward Design of MEMS Devices, NEW METHODS OF DAMAGE AND FAILURE ANALYSES OF STRUCTURAL PARTS, Sept. 2022. (Oral)

6. Yiming Jiang, Chun-Yi Chen, Tomoyuki Kurioka, Daisuke Yamane, Masanori Mizoguchi, Osamu Kudo, Ryu Maeda, Masato Sone, Tso-Fu Mark Chang. Ultra-High Mechanical Strength and Thermal Stability of Electrodeposited Ni-B Alloys toward MEMS Micro-Components, 48th international conference on Micro and Nano Engineering - Eurosensors (MNE-ES), Sept. 2022.
7. Yiming Jiang, Chun-Yi Chen, Xun Luo, Daisuke Yamane, Masanori Mizoguchi, Osamu Kudo, Ryu Maeda, Masato Sone, Tso-Fu Mark Chang. Micro-compression and micro-hardness of electrodeposited Nickel-Cobalt alloys, 3-day International Conference on Materials Science, Oct. 2022.

Awards:

1. Best Poster Award, International Thin Films Conference, Taiwan Association for Coating and Thin Film Technology (TACT) 2021, Nov. 2021.

2. Research Fellow, Institute of Innovative Research, Tokyo Tech, Oct. 2021-Sep. 2023

3. Tsubame Scholarship, Tokyo Tech. Oct. 2021-Sep. 2023.

Acknowledgements

It is lucky for me to study at Tokyo Institute of Technology for my doctor degree. The four-year is a long journey and will be a special and fantastic experience in my life. Many people helped me along the way that I can't express my highest appreciate to all of them.

First and foremost, I would like to express my deepest gratitude to Professor Masato Sone and Professor Tso-Fu Mark Chang for their guidance. They were so kind to me when I first met them, so I could quickly start my research and get used to the life in Japan. They gave me countless valuable advice in my academic research. Thanks to their help and encouragement, I could have learned about how to do research and improve my academic skills.

I want to deeply thank Assistant Prof. Tomoyuki Kurioka Mrs. Toda for their support in administration and academic. I would not able to finish all those complex document works without their kind help. I would also like to thank my excellent teachers in Tokyo Tech and every member in Sone laboratory, Mr. Nitta, Mr. Tokuoka, Mr. Cheng, Mr. Suzuki, Mr. Iriya, Mr. Hotta, Mr. Fujita, Mr. Wu, Mr. Kawakami, Mr. Akiyama, Mr. Omura, Mr. Okamoto and Mr. Hori, thank you for helping me with my academic work and life. It is really nice to study and work in this laboratory. Special thanks to Professor Chen, Professor Yamane and Mr. Chien for their support in my experiments and daily life.

Lastly, I would like to express my thank and love to my family. They always agree with my choice and help me both financially and mentally. Their selfless love is my most precious gift.

2023.05.16

Yiming Jiang